Impact of the Summer Atmospheric Heat Source over the Tibetan Plateau on Interannual Variability of Meridional Circulation on the North Side of the Tibetan Plateau

HONGYU LUO,[a,b,c] HAIPENG YU,[a,b] ZEYONG HU,[a,b] JIE ZHOU,[d] BOFEI ZHANG,[a,b,c] YAOXIAN YANG,[e] SHANLING CHENG,[d] YONGQI GONG,[d] AND YU REN[d]

[a] *Key Laboratory of Cryospheric Science and Frozen Soil Engineering, Northwest Institute of Eco-Environment and Resources, Chinese Academy of Sciences, Lanzhou, China*
[b] *Nagqu Plateau Climate and Environment Observation and Research Station of Tibet Autonomous Region, Nagqu, China*
[c] *University of Chinese Academy of Sciences, Beijing, China*
[d] *College of Atmospheric Sciences, Lanzhou University, Lanzhou, China*
[e] *Laboratory of Climate Resource Development and Disaster Prevention, Lanzhou Resources and Environment Voc-Tech University, Lanzhou, China*

(Manuscript received 3 October 2023, in final form 4 February 2024, accepted 11 March 2024)

ABSTRACT: The summer atmospheric heat source (AHS) over the Tibetan Plateau (TP) induces meridional circulations in TP and its surrounding areas. Previous studies mainly focused on the monsoon circulation on the south side of TP, while the formation and maintenance mechanisms of meridional circulation on its north side remain unclear. This study compared three calculation methods of the AHS, analyzed the spatial–temporal variability of the summer AHS over the TP, and discussed its influence on the interannual variability of meridional circulation on the north side of the TP based on the two-dimensional decomposition method of atmospheric circulation and sensitivity experiments. The results indicate that in the positive AHS anomalies years, the diabatic heating of condensation latent release in southeastern TP could motivate anomalous ascending motion. Simultaneously, the increased meridional temperature gradient between the mid- and high latitudes of East Asia leads to an enhanced southward westerly jet. In this context, the region on the north side of TP, located on the north side of the westerly jet entrance, is affected by negative anomalous relative vorticity advection, prevailing anomalous descending motion, which makes the descending branch of meridional circulation significantly presented. Unlike previous studies that considered the descending branch of meridional circulation as the compensation for upward flow, the results of the linear baroclinic model (LBM) verify that the descending branch is mainly influenced by the vorticity advection related to regional scale variability of the westerly jet. This study reveals the physical mechanism of meridional circulation on the north side of TP, which offers valuable implications for seasonal forecasting in TP and Northwest China.

KEYWORDS: Complex terrain; Atmospheric circulation; Streamfunction; Vertical motion; Summer/warm season; Interannual variability

1. Introduction

The atmospheric heat source (AHS) is the fundamental driver of atmospheric circulation, reflecting the heat budget of the atmospheric column in a given area and time period (Ye and Gao 1979). The Tibetan Plateau (TP), with an average elevation exceeding 4000 m, serves as the most powerful AHS in the Northern Hemisphere and has significant implications for both regional and global atmospheric circulation and climate. The unique geography and high elevation of the TP make it particularly susceptible to enhanced warming effects compared to surrounding regions (You et al. 2020). Therefore, the thermal effect of the TP has become an important scientific issue.

The thermal forcing of the TP substantially influences atmospheric circulation in the TP and its surrounding areas. Earlier studies (Flohn 1957; Ye et al. 1957) established the TP as an elevated AHS in summer, with the prevalent upward flow, leading to the "monsoon circulation," which is a meridional circulation opposite to the Hadley cell in the South Asian monsoon region. In recent decades, more studies have emphasized the regulatory role of the summer AHS over the TP in monsoon circulation on the south side of the TP. Wu et al. (1997) put forward the concept of a "sensible heat driven air pump" by using Ertel's potential vortex theory and thermal adaptation theory. They argued that intense sensible heat (SH) over the TP in summer generates positive vorticity near the surface, leading to convergence, while inducing negative vorticity and divergence at the top of the troposphere. This mechanism acts as an air pump that regulates the formation and variability of the Asian summer monsoon through vertical motion and moisture transport (Wu et al. 2012; Xu et al. 2013; Wu et al. 2015, 2018; He et al. 2019; Duan et al. 2020). However, in addition to the monsoon circulation on the south side of the TP, some scholars note the existence of the meridional circulation on the north side of the TP, and the arid region of Northwest China (NWC) falls under the impact of this circulation (Ye et al. 1957). Qian et al. (2001) termed it the "arid meridional circulation" and observed

Corresponding author: Haipeng Yu, yuhp@lzb.ac.cn

DOI: 10.1175/JCLI-D-23-0599.1

significant differences in vertical circulation between dry and wet years in NWC in summer. In wet years, the ascending motion over the TP was stronger, and upward flow prevailed over the entire troposphere in NWC. While in dry years, the ascending motion over the TP was weaker, and a sinking flow that was stronger than that in normal years prevailed in the middle–upper troposphere in NWC (Wu and Qian 1996). Wei et al. (2009) also found that in July of greater precipitation years in eastern NWC, a stronger meridional circulation caused this region within the enhanced upward flow (40°–43°N), favoring precipitation. Conversely, in July of fewer precipitation years, the region fell under a closed circulation opposite to wet years, dominated by a descending motion (41°–44°N), leading to reduced precipitation. However, current studies about the meridional circulation on the north side of the TP have only focused on its spatial structure and interannual relationship with summer precipitation in NWC, while its formation and maintenance mechanisms remain unclear.

Previous studies have shown that the thermal effect of the TP is closely related to the meridional circulation on the north side of the TP, and the descending branch of meridional circulation is considered to compensate for the upward flow over the TP induced by thermal forcing. Early scholars (Wu and Qian 1996) used the surface temperature anomaly index to characterize the thermal conditions of the TP, noting that a warmer surface corresponded with enhanced ascending motion in summer, promoting convergence near the surface. Subsequent studies (Fan and Cheng 2003; Sun and Liu 2021; Luo et al. 2023) further verified that the topography effect of the TP produces both the ascending motion over the TP and the compensatory descending motion on the north side of the TP based on the results of numerical experiments. While these findings are mainly related to SH near the surface due to dataset deficiency, the role of condensation latent heat (LH) in the middle–upper troposphere cannot be overlooked. In this case, the relationship between the AHS over the TP and meridional circulation on the north side of the TP is not fully understood, primarily because of the uncertainties in quantifying the intensity and variability of the AHS, which are caused by the complex topography of the TP, scarcity, and uneven distribution of observational stations (Wang et al. 2012; Duan et al. 2014; Wu et al. 2017). Additionally, methodological discrepancies further complicate the estimation of the AHS. For instance, the bias of the direct calculation method is attributed to components such as the variations of drag coefficients in SH calculating (Duan and Wu 2008; Yang et al. 2010) and the uncertainties of satellite radiation data, while the indirect calculation method varies greatly due to the deviations between different reanalysis datasets (Luo and Xu 2019). At present, accurately estimating the AHS over the TP remains a challenge, which significantly constrains the current understanding of the underlying physical mechanisms of the summer AHS over the TP affecting the interannual variability of meridional circulation on the north side of the TP. How the summer AHS over the TP affects the meridional circulation on the north side of the TP and whether the descending branch of meridional circulation compensates for the upward flow over the TP require further exploration.

In this study, we aim to answer the following questions: 1) What are the spatial and temporal variation characteristics of the summer AHS over the TP? 2) How does the summer AHS over the TP affect the interannual variability of meridional circulation on the north side of the TP? 3) What are the formation and maintenance mechanisms of the descending branch of the meridional circulation? The remainder of this paper is organized as follows. In section 2, we briefly describe the data, methods, and model we applied. Section 3 presents the spatial and temporal variation characteristics of the summer AHS over the TP. In section 4, we first explore the relationship between the summer AHS over the TP and meridional circulation on the interannual time scale and the corresponding physical mechanism and then conduct the sensitivity experiments using the model. Finally, the conclusions and discussion are given in section 5.

2. Data and methods

a. Data

Previous studies have compared the performances of different reanalysis datasets to calculate the AHS over the TP. Hu and Duan (2015) found that the Japanese 55-year Reanalysis (JRA-55) closely resembled the observed data when calculating the summer AHS over the TP by comparing JRA-55, ERA-Interim, and NCEP-2. Wang et al. (2019) compared the differences in the variability of the summer AHS over the TP calculated from four reanalysis datasets (NCEP-1, NCEP-2, ERA-Interim, and JRA-55) and found that for long-term trends and interannual scales, JRA-55 was more consistent with the variability of the observed data. Duan and Zhang (2022) also noted that the intensity and variability calculated by JRA-55 closely matched the observed data when comparing the annual cycle of the AHS over the TP. Therefore, we used the monthly JRA-55 data from the Japan Meteorological Agency with a horizontal resolution of 1.25° × 1.25° covering the summer period (June–August) during 1981–2020 in this study (Kobayashi et al. 2015), including wind, vertical velocity, air temperature, surface pressure, total precipitation, total cloud cover (TCC), SH, radiation, and diabatic heating rate. The diabatic heating rate refers to the vertical diffusion heating rate (vdfhr), convective heating rate (cnvhr), large-scale condensation heating rate (lrghr), solar radiative heating rate (swhr), and longwave radiative heating rate (lwhr).

b. Methods

1) Atmospheric heat source

(i) Direct calculation method

This method is based on the principle of radiative balance, and the AHS is defined as

$$E = \mathrm{SH} + \mathrm{LH} + \mathrm{RC}, \tag{1}$$

where SH represents the sensible heat transfer, LH is the condensation latent heat released to the atmosphere by precipitation, and RC is the net radiative flux of the air column (W m^{-2}). Utilizing the direct calculation method can acquire the horizontal

spatial distribution of the AHS and its components, but it does not provide information on their vertical distribution.

(ii) Indirect calculation method

The method proposed by Yanai et al. (1973) initially relies on the direct vertical integration of the thermodynamic equation based on the principle of atmospheric energy conservation to calculate the AHS:

$$\langle Q_1 \rangle = \frac{1}{g}\int_{P_t}^{P_s}\left\{C_p\left[\frac{\partial T}{\partial t} + \mathbf{V}\cdot T + \left(\frac{P}{P_0}\right)^{\kappa}\omega\frac{\partial\theta}{\partial p}\right]\right\}dp, \tag{2}$$

where Q_1 refers to the diabatic heating (K s^{-1}); $\langle\ \rangle$ represents the vertical integration; P_s is the surface pressure, $P_t = 100$ hPa, and $P_0 = 1000$ hPa; T is temperature and θ is potential temperature (K); $\mathbf{V}$ is the horizontal wind vector (m s^{-1}); ω is the vertical p velocity (Pa s^{-1}); and $\kappa = R/C_p$, where R and C_p denote the gas constant and specific heat capacity of dry air at constant pressure, respectively. This method can obtain the horizontal and vertical spatial distributions of the AHS and diabatic heating but not the distribution of the components of the AHS.

(iii) Heating rate integration method

In addition, we employed the heating rate integration method to quantitatively calculate the AHS (Yu et al. 2011):

$$\begin{aligned} H &= H_{\mathrm{SH}} + H_{\mathrm{LH}} + H_{\mathrm{RC}} \\ &= \frac{1}{g}\int_{P_t}^{P_s}[C_p(\mathrm{vdfhr} + \mathrm{lrghr} + \mathrm{cnvhr} + \mathrm{lwhr} + \mathrm{swhr})]dp, \end{aligned} \tag{3}$$

where H_{SH} is the vertical integration of the vdfhr, H_{LH} represents the vertical integration of the lrghr and the cnvhr, and H_{RC} is the vertical integration of the swhr and the lwhr. This method can provide the horizontal and vertical spatial distributions of the AHS and its components depending on the availability of heating rate data.

2) REGIONAL MERIDIONAL MASS STREAMFUNCTION

The mass streamfunction is commonly used to characterize the global zonal mean meridional circulation. However, the meridional circulation over the TP exhibits significant regional characteristics (Hu and You 2019), due to the intense land–sea thermal contrast combined with the dynamic and thermal effects of the TP's large topography, and the atmospheric motion within this region cannot satisfy the zonal mean continuity equation, and a regional meridional mass streamfunction (RMMSF) is needed.

To better characterize the spatial structure of meridional circulation on the north side of the TP, we employ the two-dimensional decomposition method of the vortex and divergent circulation in fluid dynamics (Schwendike et al. 2014, 2015). For any given pressure surface, we can decompose the horizontal velocity:

$$\mathbf{V}(\lambda,\varphi,p) = \mathbf{V}_{\mathrm{div}}(\lambda,\varphi,p) + \mathbf{V}_{\mathrm{rot}}(\lambda,\varphi,p), \tag{4}$$

where $\mathbf{V}_{\mathrm{div}}$ and $\mathbf{V}_{\mathrm{rot}}$ represent the divergent (irrotational) and vortex (nondivergent) parts of the horizontal velocity, respectively. Under this condition, the continuity equation $\nabla_p\cdot\mathbf{V} + \partial\omega/\partial p = 0$ in the pressure coordinates can be reformulated as follows:

$$\nabla_p\cdot\mathbf{V}_{\mathrm{rot}} = 0, \tag{5}$$

$$\nabla_p\cdot\mathbf{V}_{\mathrm{div}} + \frac{\partial\omega}{\partial p} = 0. \tag{6}$$

Since the vertical motion is mainly induced by the horizontal divergent wind, the vortex component $\mathbf{V}_{\mathrm{rot}}$ of the horizontal velocity is often neglected. The continuity equation can then be simplified as follows:

$$\frac{1}{a\cos\varphi}\frac{\partial u_{\mathrm{div}}}{\partial\lambda} + \frac{1}{a\cos\varphi}\frac{\partial v_{\mathrm{div}}\cos\varphi}{\partial\varphi} + \frac{\partial\omega}{\partial p} = 0. \tag{7}$$

The vertical velocity is also decomposed into two components:

$$\omega = \omega_m + \omega_z, \tag{8}$$

where ω_m is the meridional vertical velocity and ω_z is the zonal vertical velocity. The continuity equation satisfied by the regional meridional circulation is as follows:

$$\frac{1}{a\cos\varphi}\frac{\partial v_{\mathrm{div}}\cos\varphi}{\partial\varphi} + \frac{\partial\omega_m}{\partial p} = 0. \tag{9}$$

To employ the mass streamfunction Ψ for the regional meridional circulation, Eq. (9) is reformulated as follows:

$$\frac{\Delta\varphi a}{g}\frac{\partial v_{\mathrm{div}}\cos\varphi}{\partial\varphi} + \frac{\Delta\varphi a^2\cos\varphi}{g}\frac{\partial\omega_m}{\partial p} = 0, \tag{10}$$

where v_{div} and ω_m can be represented by the mass streamfunction as follows:

$$v_{\mathrm{div}} = \frac{g}{\Delta\varphi a\cos\varphi}\frac{\partial\Psi}{\partial p}, \tag{11}$$

$$\omega_m = -\frac{g}{\Delta\varphi a^2\cos\varphi}\frac{\partial\Psi}{\partial\varphi}. \tag{12}$$

Given that vertical velocity is not the observing variable, we use Eq. (11) to calculate the RMMSF:

$$\mathrm{RMMSF} = \frac{\Delta\varphi a\cos\varphi}{g}\int_0^p v_{\mathrm{div}}dp, \tag{13}$$

where a is Earth's radius, g is the gravitational acceleration, and φ is the latitude. The term v_{div} can be calculated based on the relationship between the velocity potential function χ and divergent wind as $v_{\mathrm{div}} = (1/a)(\partial\chi/\partial\varphi)$.

3) DYNAMICAL DIAGNOSTIC METHOD

To explore the main influencing factors of the vertical velocity, we used the quasigeostrophic ω equation:

$$\left(\delta\nabla^2 + f_0^2\frac{\partial^2}{\partial p^2}\right)\omega = f_0\frac{\partial}{\partial p}[\mathbf{V}_g\cdot\nabla(\xi_g + f)] + \frac{R}{p}\nabla^2(\mathbf{V}_g\cdot\nabla T) - \frac{R}{C_p p}\nabla^2\frac{dQ}{dt}, \tag{14}$$

where ω is the vertical velocity, δ denotes the static stability, f_0 is the Coriolis parameter, p is the pressure, and ξ_g is the geostrophic relative vorticity; also, $\mathbf{V}_g$ represents the geostrophic horizontal wind, R is the gas constant for dry air, and T is the temperature. The terms on the right-hand side represent vorticity advection, temperature advection, and diabatic heating. By segregating each variable into a time-averaged basic state and its departure, Eq. (14) can be rewritten as follows (Peixóto and Oort 1984):

$$\begin{aligned}\left(\delta\nabla^2 + f_0^2\frac{\partial^2}{\partial p^2}\right)\omega' = f_0\frac{\partial}{\partial p}\Bigg[&\underbrace{u_g'\frac{\partial\overline{\xi_g}}{\partial x}}_{\text{V1}} + \underbrace{\overline{u_g}\frac{\partial\xi_g'}{\partial x}}_{\text{V2}} + \underbrace{u_g'\frac{\partial\xi_g'}{\partial x}}_{\text{V3}}\\ &+ \underbrace{v_g'\frac{\partial\overline{\xi_g}}{\partial y}}_{\text{V4}} + \underbrace{\overline{v_g}\frac{\partial\xi_g'}{\partial y}}_{\text{V5}} + \underbrace{v_g'\frac{\partial\xi_g'}{\partial y}}_{\text{V6}} + \underbrace{v_g'\frac{\partial f}{\partial y}}_{\text{V7}}\\ &+ \frac{R}{p}\nabla^2\Bigg(\underbrace{u_g'\frac{\partial\overline{T}}{\partial x}}_{\text{T1}} + \underbrace{\overline{u_g}\frac{\partial T'}{\partial x}}_{\text{T2}} + \underbrace{u_g'\frac{\partial T'}{\partial x}}_{\text{T3}} + \underbrace{v_g'\frac{\partial\overline{T}}{\partial y}}_{\text{T4}}\\ &+ \underbrace{\overline{v_g}\frac{\partial T'}{\partial y}}_{\text{T5}} + \underbrace{v_g'\frac{\partial T'}{\partial y}}_{\text{T6}}\Bigg) - \frac{R}{C_p p}\underbrace{\nabla^2\frac{dQ'}{dt}}_{Q}\Bigg],\end{aligned} \tag{15}$$

where V1–V7 represent the terms related to vorticity advection, T1–T6 are related to temperature advection, and Q is related to diabatic heating. The 14 terms represent the 14 factors related to the vertical velocity anomalies.

4) Cumulative anomaly test

To determine the interdecadal transition, the cumulative anomalies were calculated. The formula is (Wei 2007)

$$\hat{x}_t = \sum_{i=1}^{t}(x_i - \overline{x})(t = 1, 2, \ldots, l), \tag{16}$$

where x_i, $\overline{x}$, l, and $\hat{x}_t$ are the original time series, the average value, the length of time, and the cumulative anomaly at time t, respectively.

c. Linear baroclinic model

The linear baroclinic model (LBM) is a simple dry model based on the linearized atmospheric general circulation model developed at the Center for Climate System Research, University of Tokyo, and the National Institute for Environment Studies, Japan (Watanabe and Kimoto 2000; Watanabe and Jin 2002). This model is widely used to examine the atmospheric response to idealized diabatic heating (Lu and Lin 2009) and uses primitive equations and the triangular truncated spectral expansion method in the global domain. We employed the version with a horizontal resolution of T42 and 20 vertical layers based on a sigma coordinate system in this study, and the background basic state was calculated using the summer mean climatology based on the NCEP/NCAR reanalysis.

Suppose $\mathbf{X}$ is the vector variable in the primitive equations, and the variable can be vorticity ζ, divergence D, temperature T, and the logarithm of surface pressure π = lnPs. If disturbance $\mathbf{X} \equiv \mathbf{X}(\zeta, D, T, \pi)$, the dynamic equation of the model can be expressed as follows:

$$d_t\mathbf{X} + (L + \text{NL})\mathbf{X} = F, \tag{17}$$

where L and NL represent the linear and nonlinear parts of the formula, respectively, which can be composed of advection, geostrophic deviation, pressure gradient, and dissipation terms, and F represents the external forcing. A linear equation for the disturbance can be obtained by linearizing the equation and ignoring the nonlinear term:

$$d_t\mathbf{X}' + L\mathbf{X}' = F'. \tag{18}$$

It should be noted that the linear operator L is a function of the fundamental field, i.e., $L \equiv L(\overline{\mathbf{X}})$. Therefore, the stable solution $d_t\mathbf{X}' = 0$ in the above formula can be expressed as

$$L\mathbf{X}' = F'. \tag{19}$$

The above formula can also be expressed as a set of linear equations, and the solution is

$$\mathbf{X}' = L^{-1}F'. \tag{20}$$

The corresponding linear response solution $\mathbf{X}$ is solved by calculating the linear operator L of the primitive equation and the given external forcing F.

3. Spatial–temporal variability of the summer AHS over the TP

a. Spatial distribution

Before discussing the variability of the summer AHS over the TP, it is crucial to gain a preliminary understanding of its climatic characteristics. Figures 1 and 2 show the horizontal and vertical spatial distributions of the summer AHS over the TP and its components during 1981–2020 calculated by three methods. Horizontally, as evident in Figs. 1g–i, the AHS over the TP exhibits a spatial pattern of "strong in the south and weak in the north." Area with high value is mainly concentrated in the southeastern TP (exceeding 160 W m^{-2}), whereas the Qaidam Basin and the northern TP appear as low-value areas. Regarding the components of the AHS, the western and northern TP are dominated by SH due to scarce vegetation and exposed surface, where solar radiation reaches

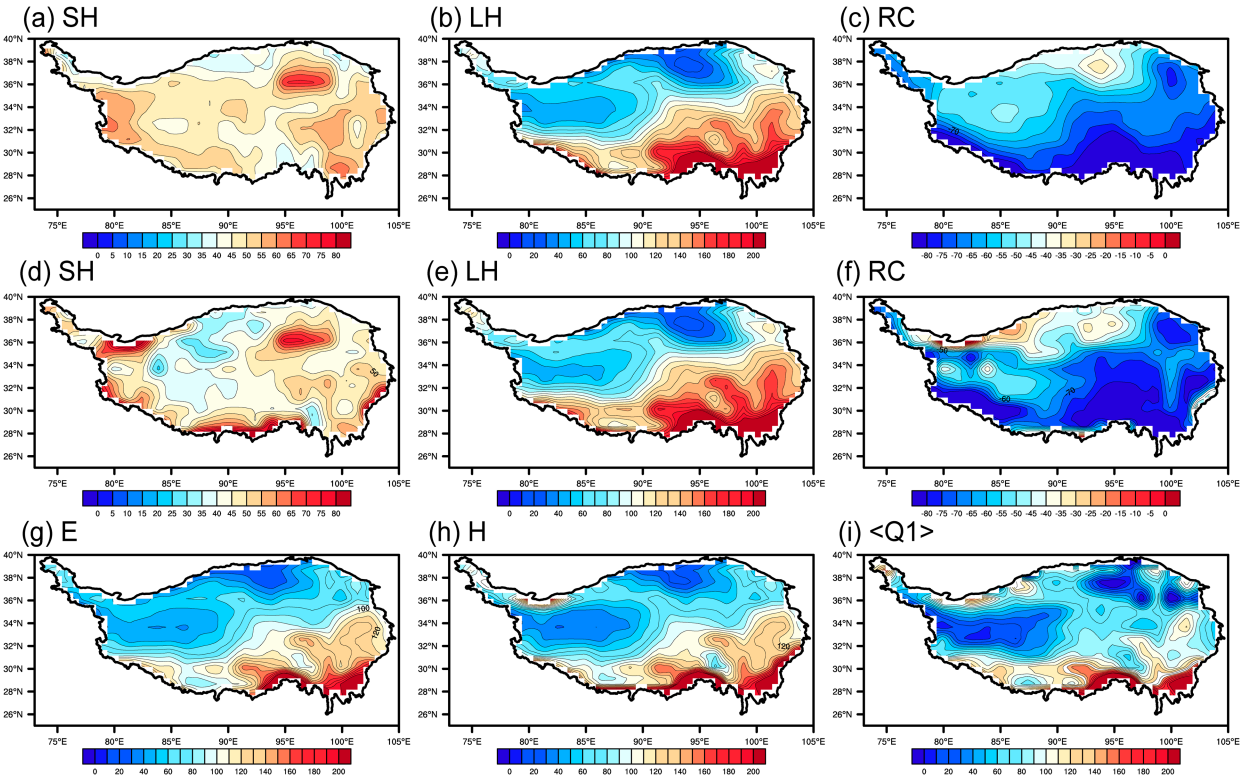

FIG. 1. Horizontal spatial distributions of the summer AHS and its components over the TP during 1981–2020. (a)–(c) SH, LH, and RC computed by the direct calculation method. (d)–(f) SH, LH, and RC calculated by the heating rate integration method. (g) AHS (E) calculated by the direct calculation method. (h) AHS (H) calculated by the heating rate integration method. (i) AHS ($\langle Q1 \rangle$) calculated by the indirect calculation method (W m^{-2}).

the surface directly, causing it to heat rapidly (Figs. 1a,d). In the eastern and southern TP, characterized by lower altitudes and ample moisture, LH released by precipitation dominates (Figs. 1b,e). Meanwhile, the RC is predominantly negative across most regions, indicating that net longwave radiative (NLR) cooling is stronger than net shortwave radiative (NSR) heating (Figs. 1c,f). Comparing the spatial distributions and magnitudes of the AHS over the TP and

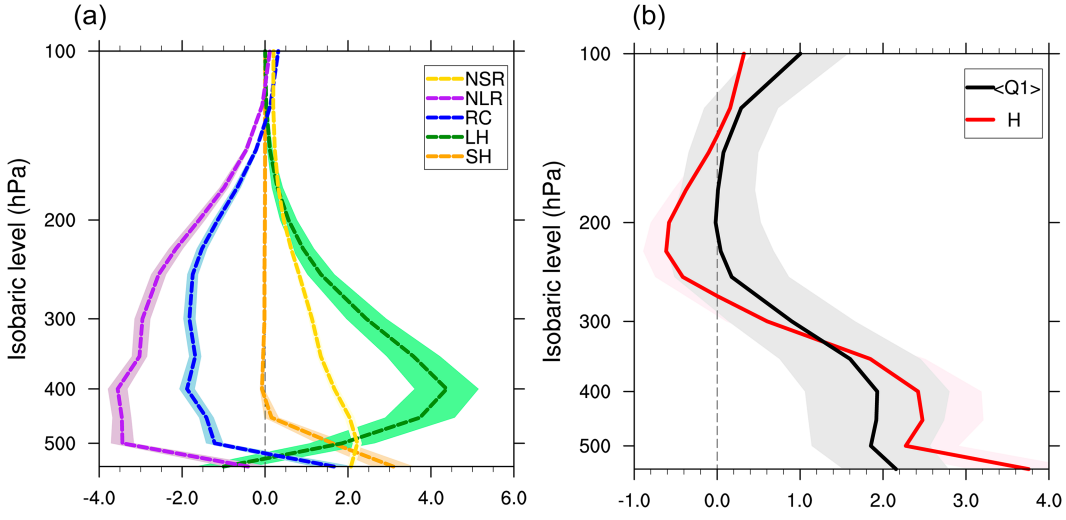

FIG. 2. Vertical profiles of the summer diabatic heating over the TP during 1981–2020. (a) SH (orange line), LH (green line), RC (blue line), NLR (purple line), and NSR (yellow line) calculated by the heating rate integration method. (b) AHS calculated by the heating rate integration method (H, red line) and by the indirect calculation method ($\langle Q1 \rangle$, black line). The shaded areas represent the 40-yr standard deviation for variables (K day^{-1}).

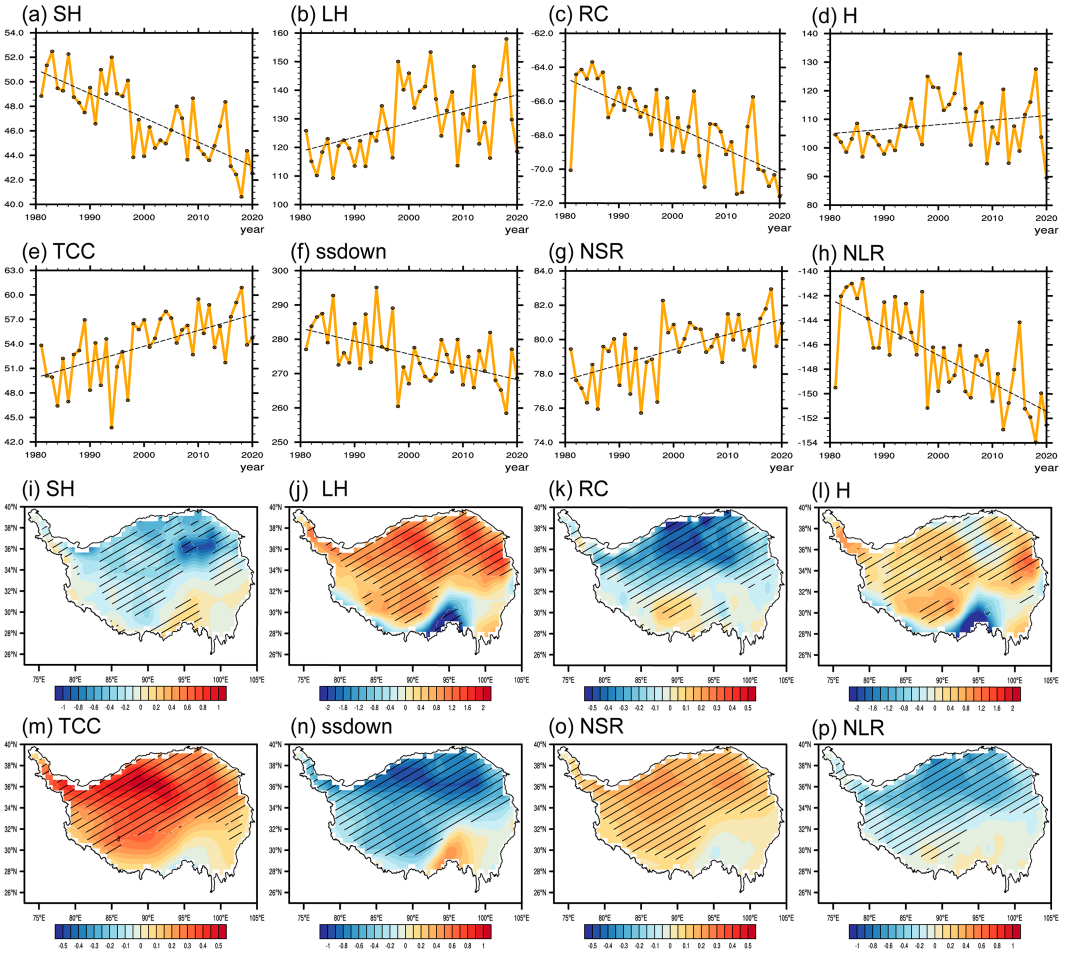

FIG. 3. (a)–(d) Time series and (i)–(l) spatial distributions of the long-term trend of the summer AHS over the TP and its components during 1981–2020. (e)–(h) Time series and (m)–(p) spatial distributions of the long-term trend of the TCC, downward shortwave radiation at the surface (ssdown), NSR, and NLR over the TP during 1981–2020. Yellow lines represent the time series, and black lines represent linear trends. The areas with diagonal lines indicate the values that passed the 95% significance test (W m^{-2}).

its components, it is evident that the AHS over the TP closely resembles the LH; therefore, we can conclude that the main contribution of the summer AHS over the TP is the LH.

It can be seen that the summer AHS over the TP shows a "⟨" vertical distribution pattern in Fig. 2b: Below 300 hPa, it is a strong heat source region, with the maximum value appearing around 400 hPa (approximately 2–3 K day^{-1}); a weak cooling source region exists at the height of 300–150 hPa, and above 150 hPa, it turns into a heat source region. As can be seen from the vertical distribution characteristics of components of the AHS (Fig. 2a), the primary contribution to the near the surface is SH, which is largely limited by its vertical transport. Owing to the correlation between LH and the phase transition process of water, regions with high values of LH are mainly distributed in the middle–upper troposphere, which is consistent with the distribution of atmospheric cloud height. Regarding the RC, shortwave radiation predominantly contributes to heating, whereas longwave radiation contributes mainly to cooling. The magnitude of NSR is smaller than that of NLR. Hence, the vertical distribution of RC is predominantly governed by NLR, with peak values similarly distributed in the middle–upper troposphere.

Furthermore, by comparing the results of different methods for calculating the AHS, it can be seen that the direct calculation method and the heating rate integration method are highly consistent in terms of both the horizontal spatial distribution and magnitude. Similarly, the indirect calculation method corresponds well with the vertical spatial distribution of the heating rate integration method, although its magnitude is slightly smaller near the surface over the TP compared to that of the heating rate integration method, which aligns with the findings of Luo and Xu (2019). Overall, considering that the heating rate integration method can correspond well with both the direct and indirect calculation methods and provide the horizontal and vertical distribution of the AHS and its components, we adopted this particular method for the subsequent calculation of the AHS over the TP.

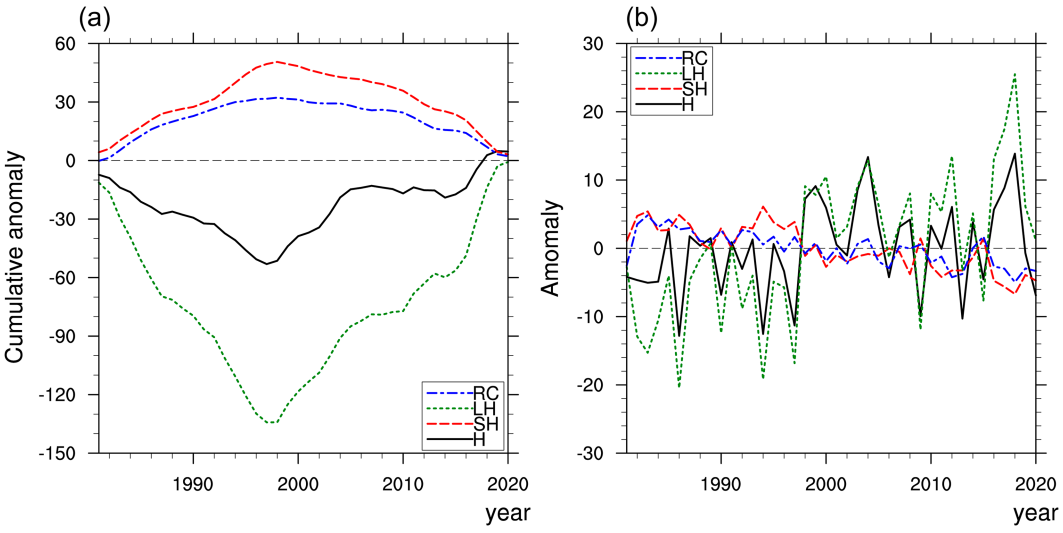

FIG. 4. (a) Cumulative anomaly series and (b) anomaly series of the summer AHS over the TP and its components during 1981–2020. Black lines represent the AHS (H), red lines represent SH, green lines represent LH, and blue lines represent RC (W m^{-2}).

b. *Temporal variability*

As a sensitive and responsive region to climate change, the TP has experienced a series of significant changes in its surface water and thermal conditions, such as glacier melting, lake expansion, and reduction in permafrost area (Sun et al. 2020; Wang et al. 2020; Zhang et al. 2020), and the consequent changes in the diabatic heating over the TP have also important impacts on regional and global atmospheric circulation. Figures 3–5 illustrate the variability of the summer AHS over the TP. As far as the long-term trend, from the time series in Figs. 3a–d, it can be observed that the AHS and LH over the TP show continuous increasing trends, with growth rates of 0.50 and 0.16 (W m^{-2} a^{-1}), respectively. On the other hand, SH and RC exhibit sustained decreasing trends, with reduction rates of 0.20 and 0.14 (W m^{-2} a^{-1}), respectively. From the spatial distribution of the trends in Figs. 3i–l, the summer AHS displays an increasing trend in most regions of the TP and a decreasing trend in the Qaidam Basin and along the Himalayas. The trends of the summer AHS across most regions of the TP are mainly driven by the variations of LH, while the decreasing trend of the summer AHS in Qaidam Basin is primarily a result of the combined effects of reduced SH and intensified radiative cooling. Regarding the components of the AHS, as indicated in Figs. 3m–p, the spatial distribution of the trend of SH exhibits a generally opposite pattern to that of TTC, which is due to the fact that the weakening effect of the atmospheric cloud on solar radiation is enhanced with an increase in TCC, resulting in a decrease in the shortwave radiation received by the surface, which weakens the surface temperature and leads to a decrease in SH. The increase in TCC also contributes to a higher moisture content in the air, leading to an opposite trend of LH to the trend of SH. As for the trend of RC, the decrease in NLR plays a major role.

In terms of interdecadal variability, as shown from the cumulative anomaly sequences in Fig. 4a, there is a significant interdecadal transition in both the summer AHS and its components during the mid-1990s. The summer AHS and LH over the TP transitioned from a weakened to enhanced trend, whereas the trends of SH and RC reversed. Related studies have shown that the interdecadal transition of the summer AHS over the TP in the mid-1990s might be associated with the Atlantic multidecadal oscillation (AMO) (Zhou et al. 2019; Sun et al. 2020; Zhang et al. 2020; Han et al. 2021). Since the mid-1990s, the AMO has been in a positive phase, with its abnormally warm sea surface temperature triggering the Silk Road pattern teleconnection, leading to a weakened and northward westerly jet (WJ) over the TP. Anomalous anticyclones in the eastern TP weaken the WJ and retain moisture over the TP, while anomalous cyclones in the western TP transport moisture from the Arabian Sea to the TP, which together have led to an increase in moisture content over the TP since the mid-1990s, and the release of LH further results in the enhancement of the summer AHS over the TP.

From the anomaly sequence in Fig. 4b, it can be observed that the summer AHS over the TP is also characterized by significant interannual variability, whose main contributor is LH, while the interannual variability of SH and RC is less obvious. Furthermore, the spatial distributions of standard deviation shown in Fig. 5 indicate significant spatial differences in the interannual variability of the summer AHS over the TP, with the center of high values of the standard deviation essentially coinciding with the climatic state. The summer AHS and LH vary more drastically in the southeastern slope of the TP, while they are relatively moderate in the northern TP, and SH varies significantly in the Qaidam Basin.

4. Impact of the summer AHS over the TP on the interannual variability of meridional circulation

a. *Climatic distribution of the meridional circulation*

For a preliminary recognition of the spatial structure of meridional circulation on the north side of the TP, we first

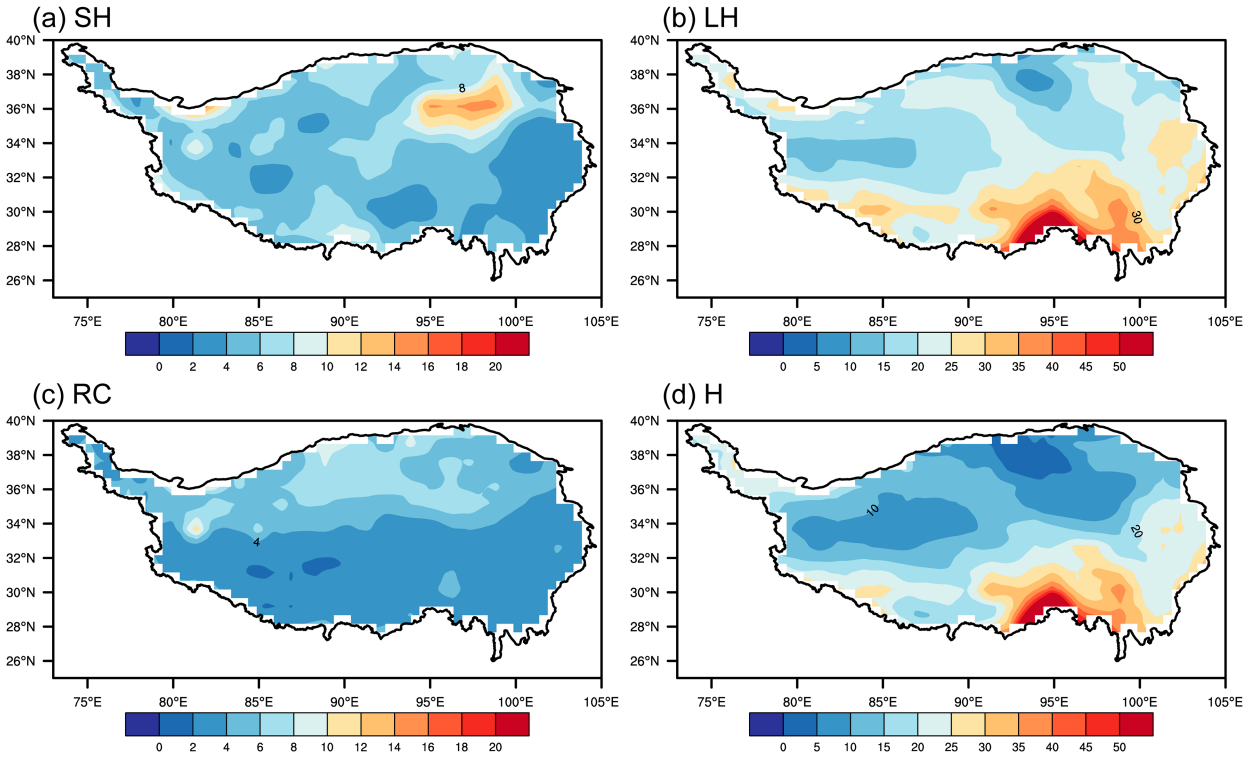

FIG. 5. Spatial distributions of the standard deviation of the summer AHS over the TP and its components during 1981–2020. (a) SH. (b) LH. (c) RC. (d) AHS (H) (W m^{-2}).

analyzed its climatic state distribution. Figure 6 illustrates the meridional circulation over the main part of the TP within the longitudinal range of 80°–100°E, where Fig. 6a shows the meridional circulation depicted by the original velocity field, while Fig. 6b shows the meridional circulation represented by the velocity field after using the two-dimensional decomposition method of atmospheric circulation. Additionally, the RMMSF was calculated for this region. When it is greater than zero, it represents a positive circulation, with a clockwise direction signifying mass transport from south to north. From the figures, it can be

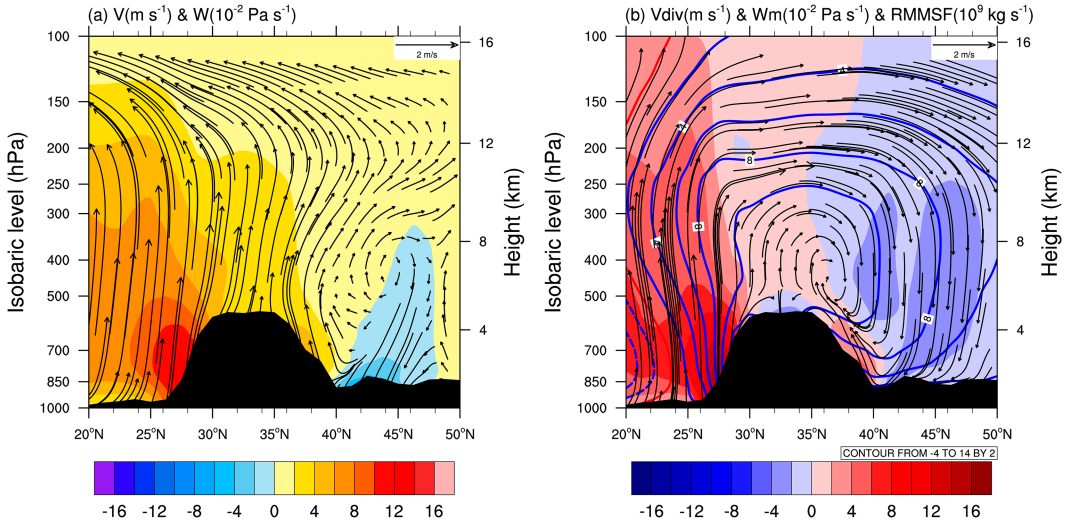

FIG. 6. Spatial distribution of the meridional circulation on the north side of the TP in summer during 1981–2020 for 80°–100°E averaged. (a) Vertical velocity (shading; 10^{-2} Pa s^{-1}) and meridional circulation (vectors; meridional wind in m s^{-1} and vertical velocity in 10^{-2} Pa s^{-1}). (b) Meridional vertical velocity (shading; 10^{-2} Pa s^{-1}), meridional circulation (vectors; meridional divergent wind in m s^{-1} and meridional vertical velocity in 10^{-2} Pa s^{-1}), and RMMSF (contours; 10^9 kg s^{-1}).

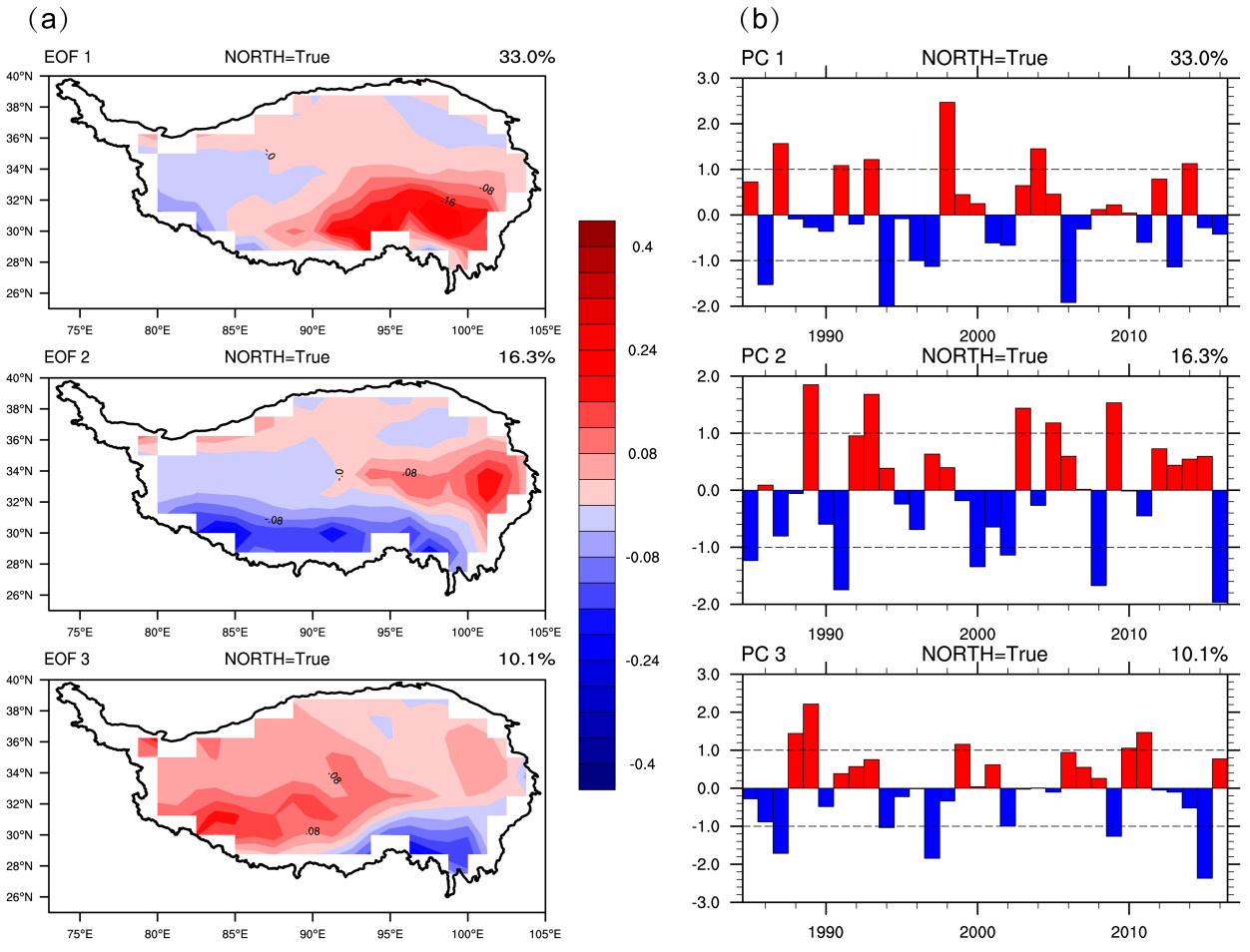

FIG. 7. The three leading EOFs of the summer AHS over the TP during 1981–2018. (a) Spatial mode. (b) Standardized time series. The percentage of explained variance by each EOF is indicated on the upper right in figures.

observed that a closed positive meridional circulation exists between 600 and 300 hPa on the north side of the TP. The airflow ascends over the TP and descends on the north side of the TP, with the center located in the arid region of NWC. Comparing Figs. 6a and 6b, it is apparent that the center of meridional circulation in Fig. 6a is approximately between 40° and 45°N, which is in agreement with previous findings (Wu and Qian 1996). In Fig. 6b, the spatial structure of meridional circulation is largely consistent with that in Fig. 6a; however, the center is slightly further south, and the spatial structure is more coherent and distinct. This suggests that zonal circulation significantly influences the vertical velocity on the north side of the TP, and the two-dimensional decomposition method of atmospheric circulation can effectively filter out its disruption, depicting a clearer and more accurate spatial structure of the meridional circulation.

b. *Relationship between the summer AHS and meridional circulation*

As established in the previous section, the variability of the summer AHS over the TP exhibits multitemporal scale characteristics. To remove the low-frequency signals and study the impact of the summer AHS over the TP on the interannual variability of meridional circulation on the north side of the TP, we detrended and filtered (using a 9-yr running mean to retain interannual signals) the summer AHS over the TP during 1981–2020 before conducting the empirical orthogonal function (EOF) analysis. Figure 7 displays the spatial distribution and standardized time series of the first three modes. The EOF1 reveals a coherent change across the whole TP, with inverse variations in only a few regions in the western and northern parts. The EOF2 and EOF3 manifest characteristics of antiphase variation of the east–west and the north–south, respectively. The explanatory variances of each mode are, respectively, 33.0%, 16.3%, and 10.1%, and the cumulative variance contribution reaches 59.4%. All three modes have passed the North test, which shows the diversity of the characteristics of interannual variability of the summer AHS over the TP. By comparison, we find the EOF1 aligns with the distribution of standard deviation and climate state of the summer AHS, with the center of anomalous change located in southeastern TP, indicating EOF1 is the predominant spatial distribution type of the interannual variability of summer AHS over the TP. Based on the first principal component (PC1), we selected the positive and negative AHS anomalies years with a

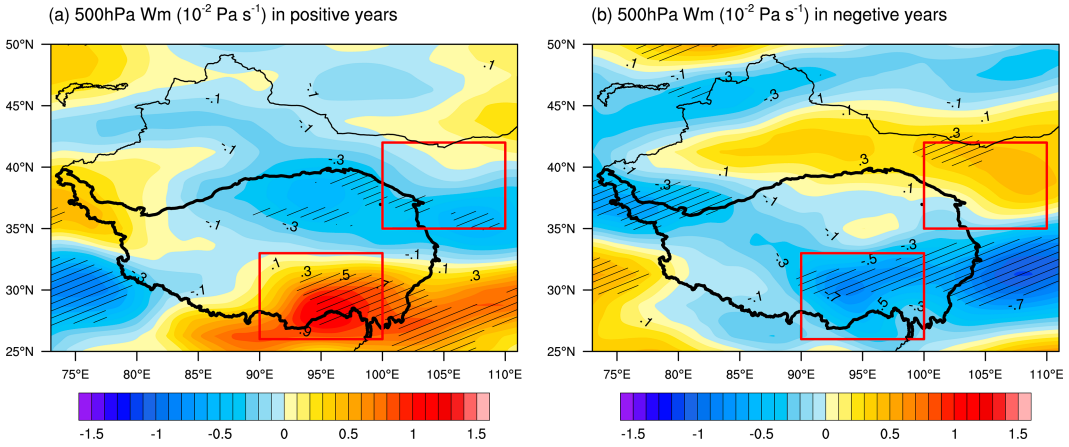

FIG. 8. Composite analysis of the 500-hPa meridional vertical velocity (shading; 10^{-2} Pa s^{-1}). (a) Positive AHS anomalies years. (b) Negative AHS anomalies years. Red boxes represent the ascending branch (26°–33°N, 90°–100°E) and the descending branch (35°–42°N, 100°–110°E) of meridional circulation on the north side of the TP. The areas with diagonal lines indicate the values that passed the 95% significance test.

threshold of one standard deviation. Specifically, we chose 6 years (1987, 1991, 1993, 1998, 2004, and 2014) as positive AHS anomalies and 6 years (1986, 1994, 1996, 1997, 2006, and 2013) as the negative AHS anomalies years. Furthermore, because the main region of the EOF1 falls within 90°–100°E, subsequent profile analyses were conducted with an average of 90°–100°E.

We conducted a composite analysis of selected positive and negative summer AHS anomalies years. Figure 8 presents the 500-hPa meridional vertical velocity over the TP and its northern areas. In the positive AHS anomalies years, anomalous ascending motion appears in the southern TP, whereas anomalous descending motion appears in the northern TP and adjacent regions, with the centers of high values mainly located in Ningxia and Shaanxi. Conversely, in the negative AHS anomalies years, anomalous descending motion dominates the entire TP, whereas anomalous ascending motion in the northern TP centered mainly in eastern Xinjiang and central Inner Mongolia. To more intuitively analyze the spatial structure of meridional circulation on the north side of the TP in response to anomalous AHS, we carried out a composite analysis of the profile within 90°–100°E (Fig. 9). When a positive anomalous AHS appears over the TP, the anomalous ascending motion prevails over the TP, while descending motion on the north side of the TP is also significantly enhanced, and the meridional circulation is obvious, with the positive RMMSF. In contrast, when a negative anomalous AHS appears over the TP, the anomalous descending motion prevails over the TP and ascending motion on the north side of the TP, with the center displaced northward and centered around 40°N. Concurrently, the meridional circulation reverses, resulting in a negative RMMSF.

To further clarify the interannual variability of the meridional circulation on the north side of the TP, we performed the EOF analysis of the RMMSF within 90°–100°E, using the same treatment as the summer AHS over the TP. The first two EOFs and corresponding PCs are presented in Fig. 10, of which the EOF1 accounts for 70.9% of the explained variance and the EOF2 for 14.2%, collectively capturing 85.1% of the total variance and thus largely representing the spatial and temporal distribution of meridional circulation on the north side of the TP. The EOF1 displays a uniform spatial pattern across the TP, centered directly over the TP, representing the overall Hadley circulation. The EOF2 shows a north–south distribution with a boundary of around 30°N, reflecting the two meridional circulations on the north and south sides of the TP, where the northern branch is wider than the southern one. EOF2 closely resembles the composite analysis of the RMMSF shown in Fig. 9, and its time series shows a 2–4-yr interannual oscillation simultaneously, indicating that the EOF2 could present the primary pattern of the meridional circulation on the north side of the TP.

We conducted a point-to-point correlation analysis between the PC2 of the EOF analysis of the RMMSF and the horizontal field of the summer AHS over the TP to further explore the correlation between the summer AHS and meridional circulation (Fig. 11a). Similarly, a correlation analysis between the PC1 of the EOF analysis of the summer AHS over the TP and the RMMSF was also carried out (Fig. 11b). As depicted in Fig. 11, a positive correlation is evident between the summer AHS over the TP and RMMSF, with a correlation coefficient reaching above 0.5 in local areas (passing the 95% significance test). Figure 11a indicates that when the meridional circulation on the north side of the TP is stronger, a positive anomalous AHS appears over the TP, centered in the southeastern TP. Fig. 11b shows that when the AHS is enhanced, the RMMSF also strengthens, implying a significantly stronger meridional circulation there, which is consistent with the above analysis.

c. *Impact of the westerly jet on meridional circulation*

The above results reveal a close correlation between the summer AHS over the TP and meridional circulation on the north side of the TP. To explore the deeper mechanism affecting the variability of meridional circulation, we applied the quasigeostrophic pressure vertical velocity ω equation to discuss the main factors related to the vertical flow anomalies over the TP and its northern regions. Based on the composite

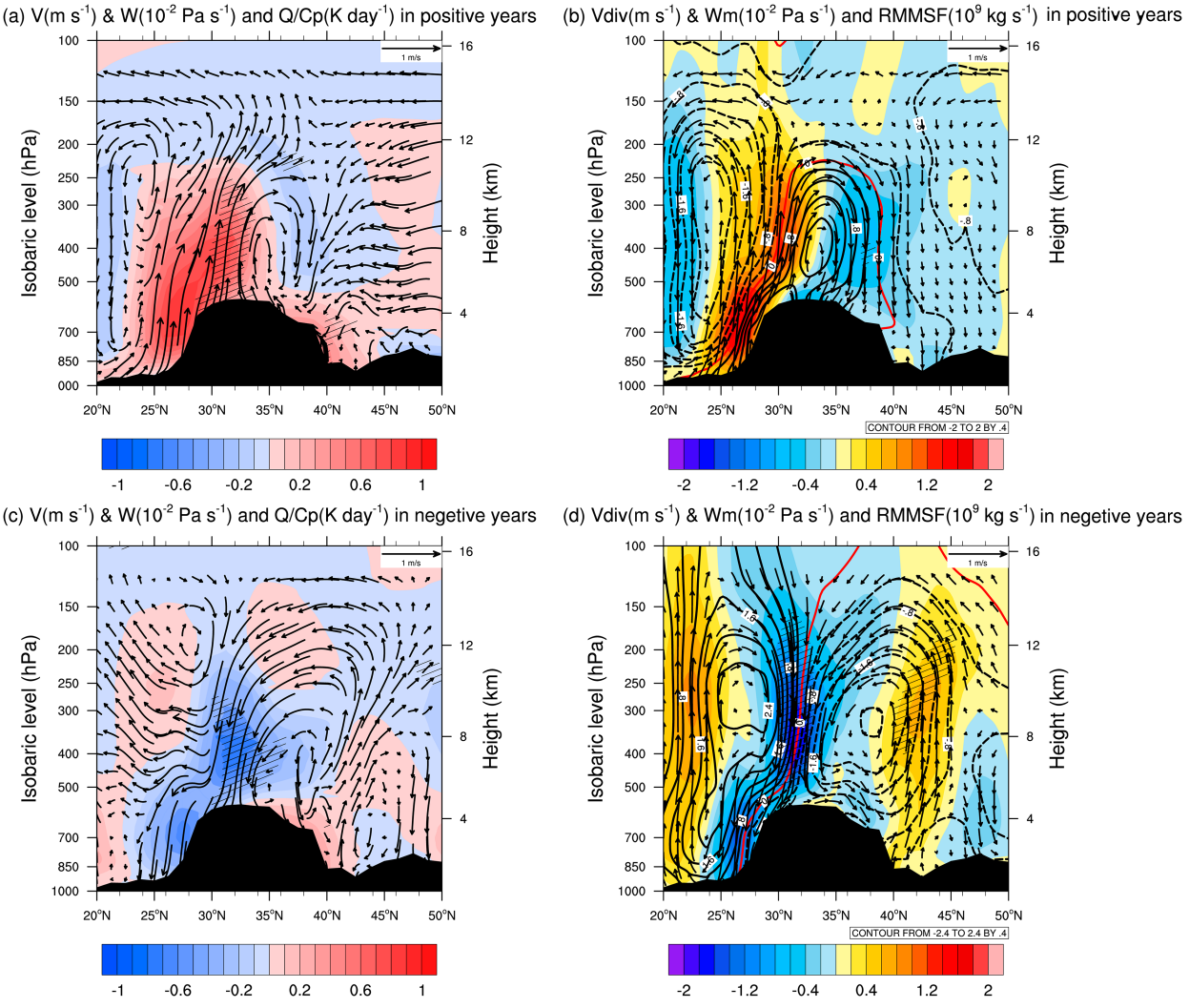

FIG. 9. Composite analysis of the vertical cross sections over the TP and its northern region for 90°–100°E averaged. (a),(b) Positive AHS anomalies years. (c),(d) Negative AHS anomalies years. (left) Diabatic heating (shading; K day^{-1}) and meridional circulation (vectors; meridional wind in m s^{-1} and vertical velocity in 10^{-2} Pa s^{-1}). (right) Meridional vertical velocity (shading; 10^{-2} Pa s^{-1}), meridional circulation (vectors; meridional divergent wind in m s^{-1} and meridional vertical velocity in 10^{-2} Pa s^{-1}), and RMMSF (contours; 10^{9} kg s^{-1}). The areas with diagonal lines indicate the values that passed the 95% significance test.

distribution of meridional vertical velocity in Fig. 8, we selected the domain of 26°–33°N, 90°–110°E that passes the significance test to characterize the ascending branch of meridional circulation and the domain of 35°–42°N, 100°–110°E to represent the descending branch. By calculating each term on the right side of Eq. (15), Fig. 12a shows that the vertical velocity anomalies of the ascending branch are mainly related to the diabatic heating Q of LH in the southeastern TP. When a positive anomalous AHS appears over the TP, the ascending motion prevails in the southeastern TP, influenced by the release of LH due to enhanced precipitation. For the descending branch (Fig. 12b), in addition to the diabatic heating Q, its vertical velocity anomalies are also closely associated with the relative vorticity advection (V2) influenced by the basic zonal flow. In the positive AHS anomalies years, anomalous descending motion in this region is primarily related to the negative anomalous relative vorticity advection; while in the negative AHS anomalies years, the anomalous ascending motion in this region is mainly associated with the positive anomalous relative vorticity advection, facilitating precipitation and the subsequent release of LH, and the diabatic heating Q also increases correspondingly.

The above diagnostic analysis confirms that the ascending branch is related to the thermal effect of the summer AHS over the TP, while the descending branch is associated with the dynamical effect of the relative vorticity advection influenced by the WJ. Is there any relationship between the WJ and the anomalous AHS over the TP? To examine that, we applied the EOF analysis to the 200-hPa zonal wind after detrending and filtering to extract the interannual signal, reflecting the meridional shift of the WJ with the EOF1

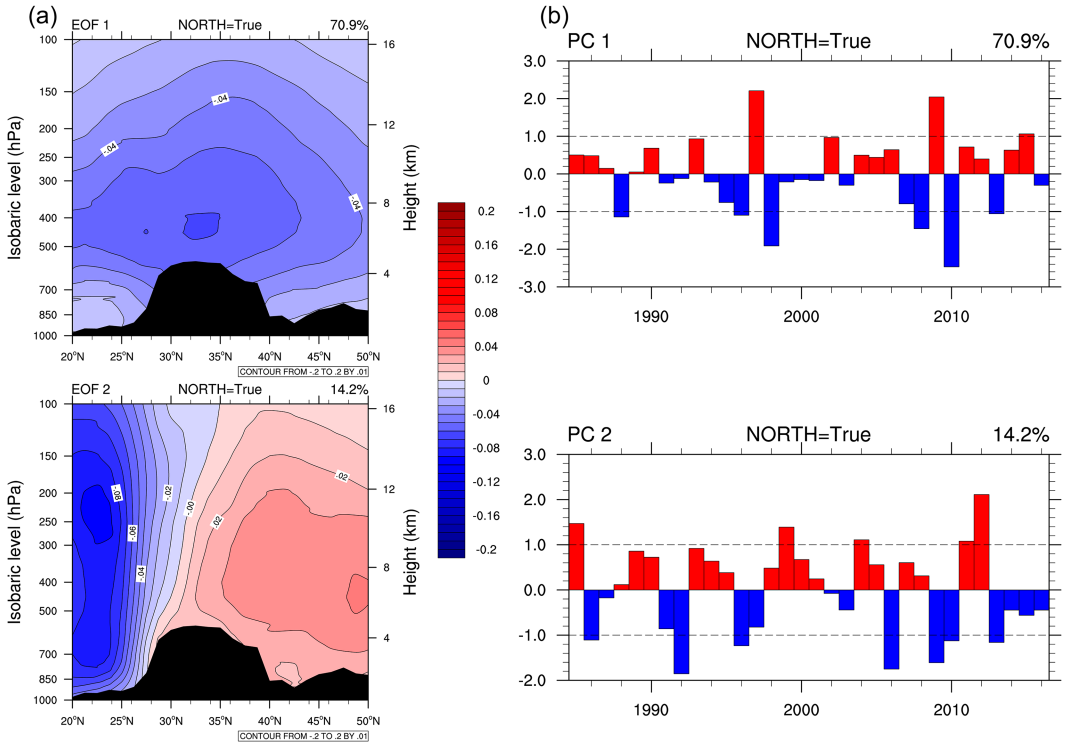

FIG. 10. The two leading EOFs of the RMMSF in summer during 1981–2018 for 90°–100°E averaged. (a) Spatial mode. (b) Standardized time series. The percentage of explained variance by each EOF is indicated on the upper right in each panel.

(Fig. 13a). The time series of the 200-hPa zonal wind and summer AHS over the TP is shown in Fig. 13b, with a correlation coefficient reaching −0.68 (passing the 95% significance level). It indicates that the shift of the WJ coincides well with the variability of the summer AHS over the TP: When the AHS is a positive anomaly, the WJ shifts southward, and when the AHS is a negative anomaly, it shifts northward.

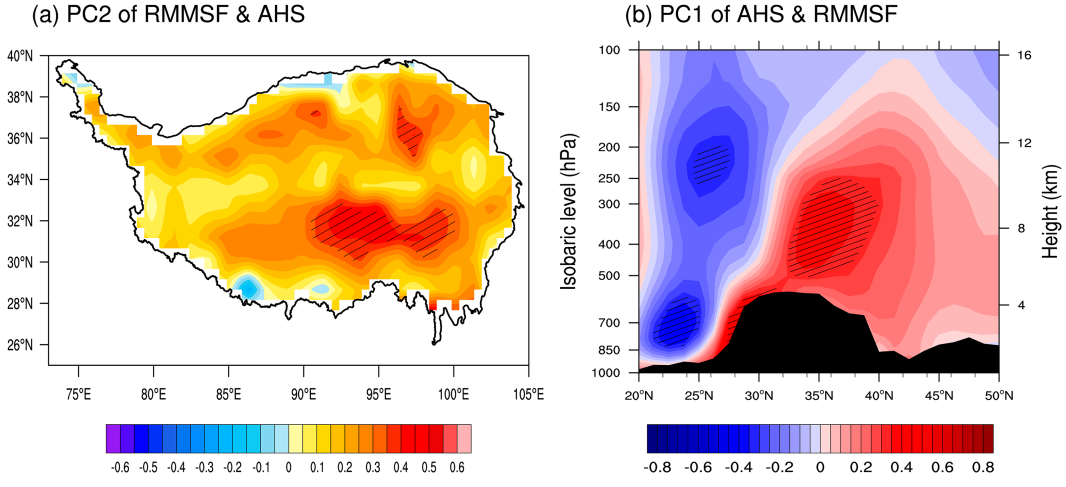

FIG. 11. Correlation relationship between the summer AHS over the TP and the meridional circulation on the north side of the TP. (a) The PC2 of RMMSF and the horizontal field of the summer AHS over the TP. (b) The PC1 of the summer AHS over the TP and the RMMSF. The areas with diagonal lines indicate the values that passed the 95% significance test.

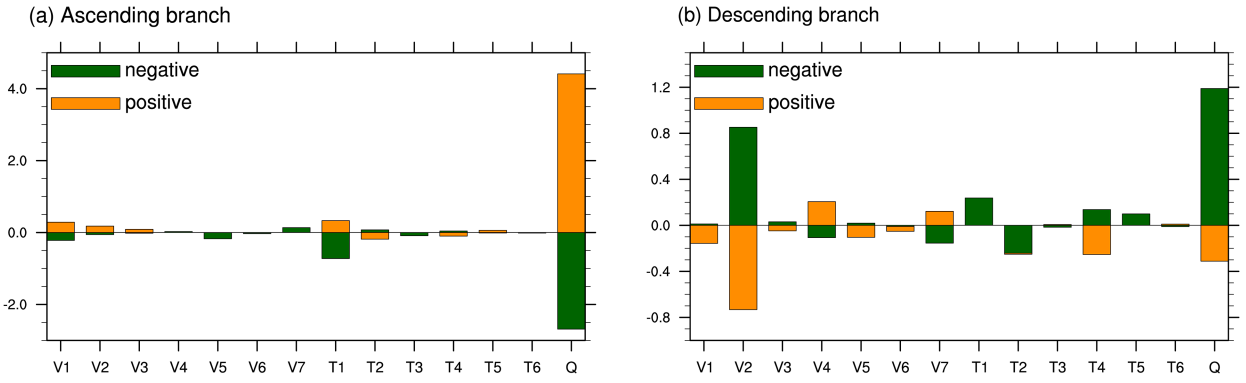

FIG. 12. The contribution analysis of the 500-hPa vertical velocity anomalies in positive and negative AHS anomalies years based on Eq. (15). (a) Ascending branch (26°–33°N, 90°–100°E) of the meridional circulation. (b) Descending branch (35°–42°N, 100°–110°E) of the meridional circulation. Labels V1–V7 represent vorticity advection, T1–T6 represent temperature advection, and Q denotes the diabatic heating (10^{-19} Pa^{-1} s^{-3}).

Further, we also present the horizontal composite distribution of 200-hPa zonal wind speed in Fig. 14. As shown in Fig. 14a, in the positive AHS anomalies years, the position of the WJ tends to the south, which is consistent with the prior analysis of Fig. 13. Based on the significant regions of the 200-hPa zonal wind speed anomalies, we give the vertical cross sections of temperature for 95°–125°E averaged (Fig. 14b) and find that the positive temperature anomalies appear over the south side of 35°N, while the negative temperature anomalies appear over the north side of 35°N, which means that the meridional temperature gradient in the mid- and high latitudes increases. According to the formation principle of thermal wind, the strength of the WJ is proportional to the temperature gradient; therefore, the WJ will enhance correspondingly, as shown by the zonal wind speed at 200 hPa in Fig. 14b. In conclusion, in the positive AHS anomalies years, there is an enhanced and southward WJ. At this time, the region of the north side of the TP (red box area in Fig. 14) is situated on the north side of the WJ entrance, affected by negative anomalous relative vorticity advection, prevailing abnormal descending motion. While in the negative AHS anomalies years, the opposite is true (Figs. 14c,d).

d. *Numerical experiments*

To confirm our findings regarding the impact of the summer AHS over the TP and vorticity advection related to the WJ on interannual variability of meridional circulation on the north side of the TP, we employed the LBM to conduct sensitivity experiments. Figures 15a and 15c show the spatial distribution of the difference field of the AHS and relative vorticity between the positive and negative AHS anomalies years. The large value area of AHS anomalies is primarily concentrated in the southeastern TP (box Q in Fig. 15a). The anomalous

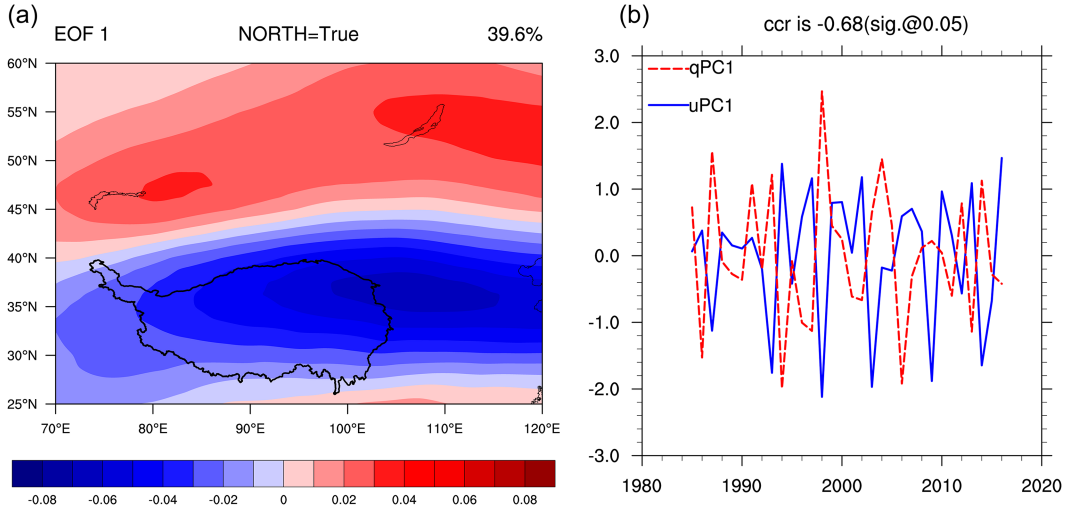

FIG. 13. Relationship between the AHS over the TP and the WJ. (a) The EOF1 derived from the EOF analysis of the 200-hPa zonal wind. (b) Time series of the PC1 of the AHS over the TP (red line) and the PC1 of the 200-hPa zonal wind (blue line) in summer during 1981–2020.

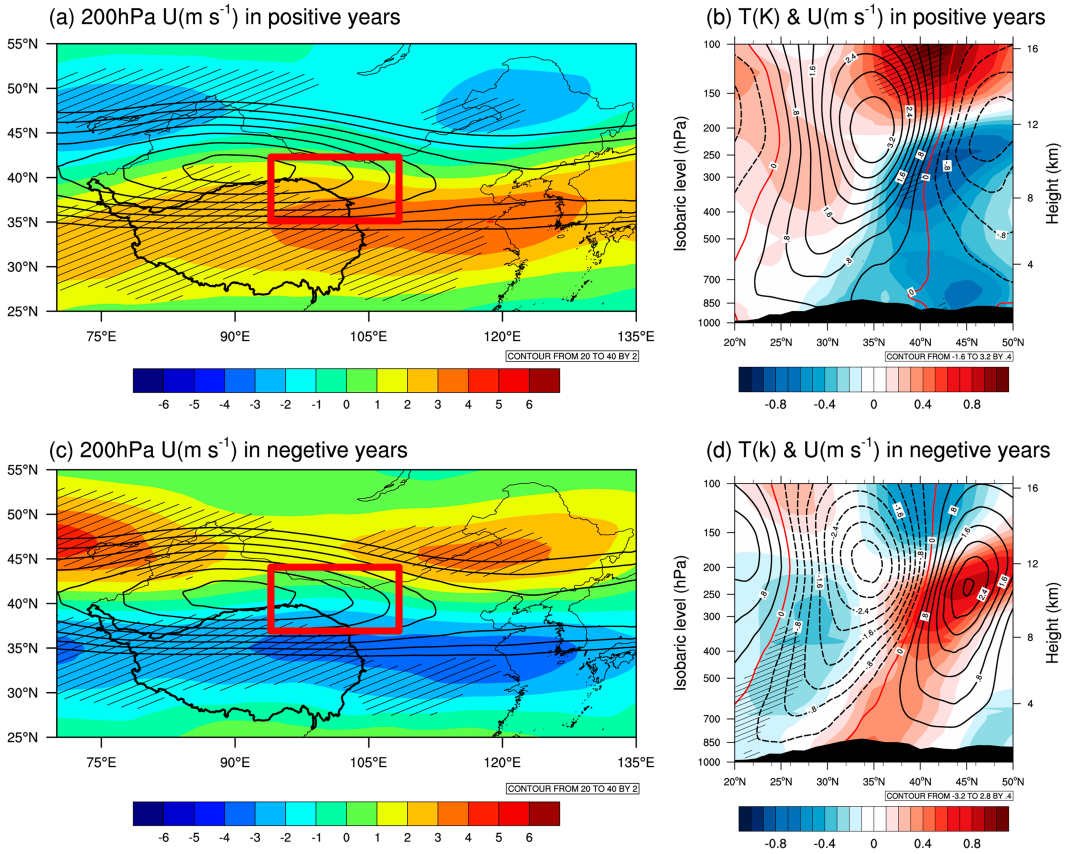

FIG. 14. Composite analysis of the 200-hPa zonal wind and vertical cross sections of zonal wind and temperature for 95°–125°E averaged in summer during 1981–2020. (a),(b) Positive AHS anomalies years. (c),(d) Negative AHS anomalies years. (left) The 200-hPa zonal wind speed (shading, anomaly; contours, climatology; m s^{-1}). (right) Temperature (shading; K) and zonal wind speed (contours; m s^{-1}). The areas with diagonal lines indicate the values that passed the 95% significance test, and the red boxes represent the descending branch of the meridional circulation.

vorticity mainly exhibits a distribution with positive at the north side and negative at the south side of the WJ core along 35°N (boxes V1 and V2 in Fig. 15c), indicating the regional scale variability of the WJ. The vertical profiles of the significant areas of anomalous diabatic heating (black box in Fig. 15a) and relative vorticity (red and blue boxes in Fig. 15c) are also shown in Figs. 15b and 15d, where the peak of diabatic heating is distributed at 400 hPa and the peak of vorticity at 200 hPa.

Based on the locations and intensities shown in Fig. 15, we added the corresponding diabatic heating forcing and vorticity forcing to the LBM. Three sets of sensitivity experiments are designed as follows: adding only the diabatic heat forcing (LBM–Q, Fig. 16a), adding only the vorticity forcing (LBM–V, Fig. 16e), and adding both the two forces at the same time (LBM–QV, Fig. 16i). The model was integrated for 50 days using the time integration method, and the average of the last 20 days was analyzed to study the steady atmospheric circulation response to the heat source forcing and vorticity forcing.

The circulation responses of the three experiments are given in Fig. 16. The results of the three experiments indicate the following: 1) When only adding the heat source forcing over the TP, the simulated WJ anomalies (Fig. 16b) can only correspond over the TP compared with Fig. 14a, and the magnitude is small, indicating that the influence of the AHS over the TP on the WJ has regional limitations. From the results of vertical velocity (Figs. 16c,d), it can be seen that the AHS over the TP can stimulate strong ascending motion of meridional circulation, but the simulation effect of descending motion is poor, indicating the AHS over the TP has limited influence on the descending branch. 2) When only vorticity forcing is added, most of the simulated WJ anomalies (Fig. 16f) can correspond to Fig. 14a, but there is a slight difference over the TP. Simultaneously, the anomalous descending motion prevails on the north side of the TP (Figs. 16g,h), which indicates that the vorticity advection related to the WJ has a great effect on the descending branch of meridional circulation. 3) Finally, when we add both vorticity forcing and heat source forcing, the model well simulates the WJ anomalies and vertical velocity distribution in the reanalysis data (Figs. 16j–l), suggesting that the descending branch of meridional circulation is influenced by the comprehensive influence of the "compensation effect" of the AHS over the TP and the dynamic vorticity advection related to the WJ. In addition, we also designed three sets of negative anomaly experiments, with the distribution of AHS and

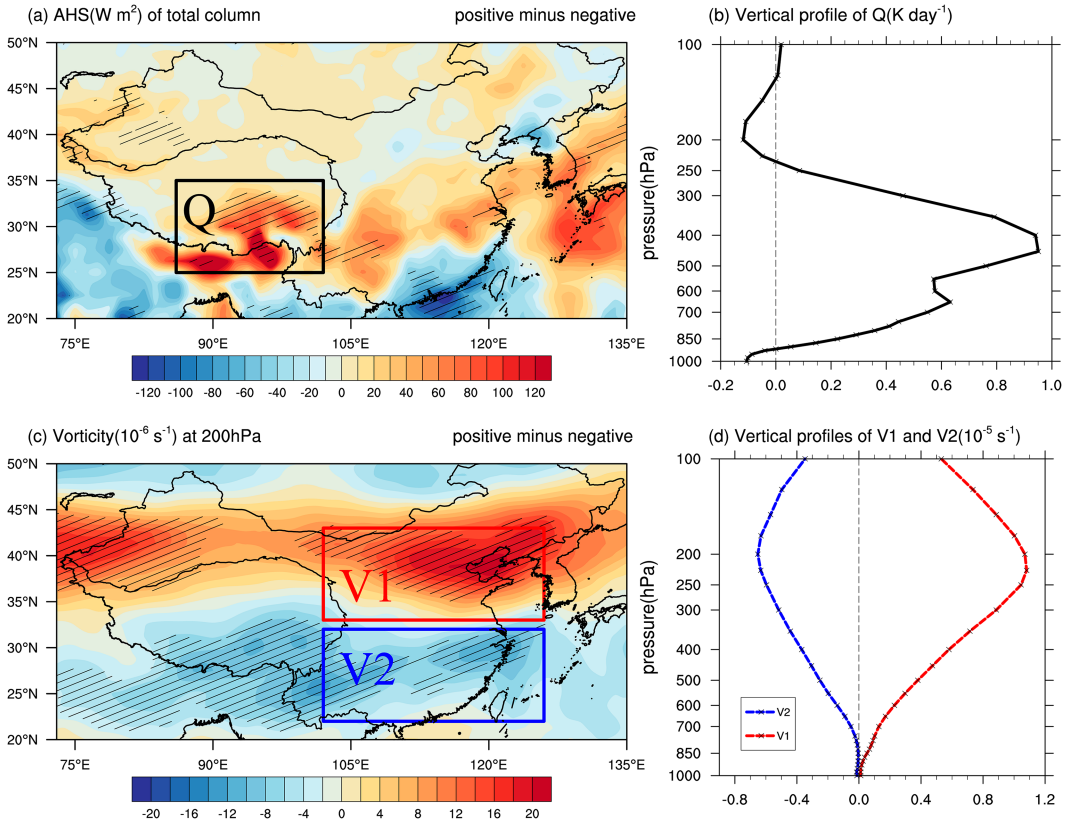

FIG. 15. The horizontal distribution of difference field of (a) the AHS of the total column (W m^{-2}) and (c) relative vorticity at 200 hPa (10^{-6} s^{-1}) between positive and negative AHS anomalies years. The vertical profiles of (b) the diabatic heating (K day^{-1}) of the "*Q*" area and (d) relative vorticity (10^{-5} s^{-1}) of the "V1" and "V2" areas. The areas with diagonal lines indicate the values that passed the 95% significance test. Black (25°–35°N, 86°–102°E), red (33°–43°N, 102°–126°E), and blue (22°–32°N, 102°–126°E) boxes represent the regions where heat source forcing and positive and negative vorticity forcing are added in the LBM, respectively.

relative vorticity opposite to the positive anomaly experiments (not shown), and the results of the circulation responses are almost inverse.

To sum up, the sensitivity experiments that distinguish causality indicate that the AHS over the TP has a significant impact on the ascending branch of meridional circulation, while its influence on the descending branch is relatively limited; vorticity advection associated with the WJ notably affects the descending branch; and the combined influence of the AHS over the TP and vorticity advection on the descending branch is most significant. Besides, it is important to note that this linear model adopts an idealized distribution of the forcing and inaccurate terrain. Consequently, the simulated circulation responses may have deviated from the reanalysis results, but they still qualitatively validate the physical mechanism affecting the interannual variability of meridional circulation on the north side of the TP.

5. Conclusions and discussion

Based on the JRA-55 during 1981–2020, we compared three calculation methods of the AHS, analyzed spatial–temporal variability of the summer AHS over the TP, and discussed its influence on interannual variability of meridional circulation on the north side of TP based on the two-dimensional decomposition method of atmospheric circulation and sensitivity experiments. The following conclusions are drawn:

1) Comparing the results of the three calculation methods of the AHS, we find that the heating rate integral method effectively captures the horizontal distribution and vertical structure of the AHS and its components and corresponds to the results of both the direct and indirect methods, making it particularly applicable in TP regions.
2) For the long-term trend, the summer AHS and LH over the TP show continuously increasing trends, whereas SH and RC exhibit decreasing trends. In terms of interdecadal and interannual variability, the main contributor to their anomalous variation is the LH. The summer AHS over the TP has an interdecadal transition in the mid-1990s and also exhibits a significant interannual variability, with the most severe changes occurring in the southeastern TP.
3) A closed meridional circulation exists between 600 and 300 hPa over the northern TP, with its sinking center located in the arid region of NWC. The results of the composite and correlation analyses indicate that when the summer AHS

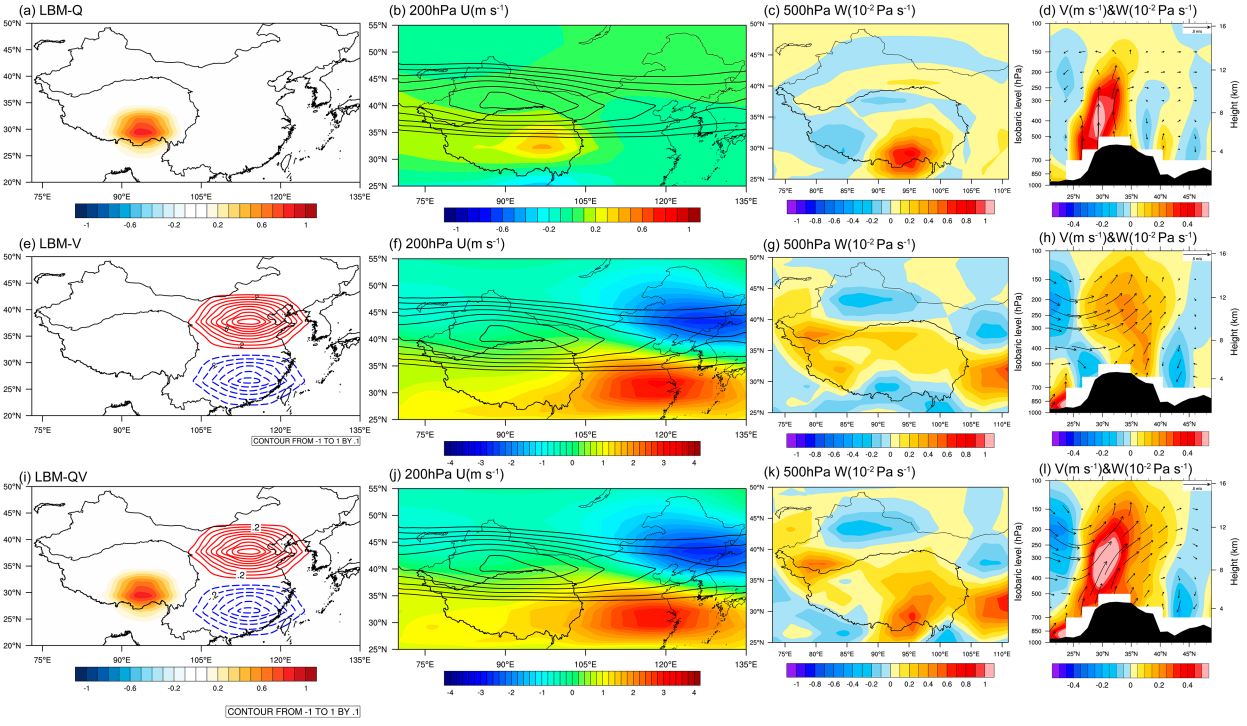

FIG. 16. Spatial distribution of heat source forcing ($\sigma = 0.4$; shading; K day^{-1}) and vorticity forcing ($\sigma = 0.2$; contours; 10^{-5} s^{-1}) in the (a) LBM-Q, (e) LBM-V, (i) LBM-QV experiments, and circulation responses of the three experiments [(b)–(d) LBM-Q, (f)–(h) LBM-V, and (j)–(l) LBM-QV]. (second column) 200-hPa zonal wind speed (shading, anomaly; contours, climatology; m s^{-1}); (third column) 500-hPa vertical velocity (shading; 10^{-2} Pa s^{-1}); (last column) meridional circulation (vectors; meridional wind in m s^{-1} and vertical velocity in 10^{-2} Pa s^{-1}).

over the TP is abnormally enhanced, anomalous ascending motion appears in the southeastern TP, whereas anomalous descending motion appears in the northern TP and adjacent regions, leading to significantly enhanced meridional circulation. Using the quasigeostrophic ω equation, we find that the anomalous vertical velocity of the ascending branch of meridional circulation is mainly related to the diabatic heating of LH in the southeastern TP, while the descending branch is closely associated with the anomalous relative vorticity advection influenced by the WJ. The positive anomalous AHS over the TP corresponds to the increase in the meridional temperature gradient between the mid- and high latitudes of East Asia, resulting in an enhanced and southward WJ. At this time, the region of the north side of the TP, located on the north side of the WJ entrance, is affected by negative anomalous vorticity advection, prevailing anomalous descending motion.

4) Previous studies considered the descending branch of meridional circulation on the north side of the TP as the compensation of the upward flow (Qian et al. 2001; Liu et al. 2007; Sun and Liu 2021; Luo et al. 2023), whereas the sensitivity experiments that distinguish causality of LBM verified the limitation of the compensation effect of the AHS over the TP. The descending branch of meridional circulation is mainly influenced by the "dynamic effect" of anomalous vorticity advection related to the regional scale variability of the WJ. The above mechanism of interannual variability of meridional circulation on the north side of the TP is shown in Fig. 17.

There are still some limitations in the process of exploring the mechanism of the influence of the summer AHS over the TP on the interannual variation of meridional circulation on the north side of the TP. First, we used the traditional two-dimensional decomposition method of atmospheric circulation to analyze the spatial structure of meridional circulation, which artificially ignores the influence of horizontal vortex component on vertical–meridional motion, presenting certain theoretical bias (Hu et al. 2020). Moreover, regarding the high correlation of the AHS over the TP and the regional variability of WJ (Fig. 13b), the mechanism is complex and needs further discussion. On the one hand, the AHS over the TP can affect the local variability of the WJ by influencing the meridional temperature gradient over the TP. On the other hand, the AHS over the TP is also regulated by the WJ because the TP is situated on the south side of the westerlies. In addition, both the AHS over the TP and the variability of WJ are also affected by the upstream propagated Rossby wave train. Previous studies have indicated that the North Atlantic Oscillation (Liu et al. 2015; Wang et al. 2017, 2018; Shang et al. 2021) and sea surface temperature (SST) anomalies in the North Atlantic can affect the interannual variability of precipitation and AHS over southeastern TP by exciting the large-

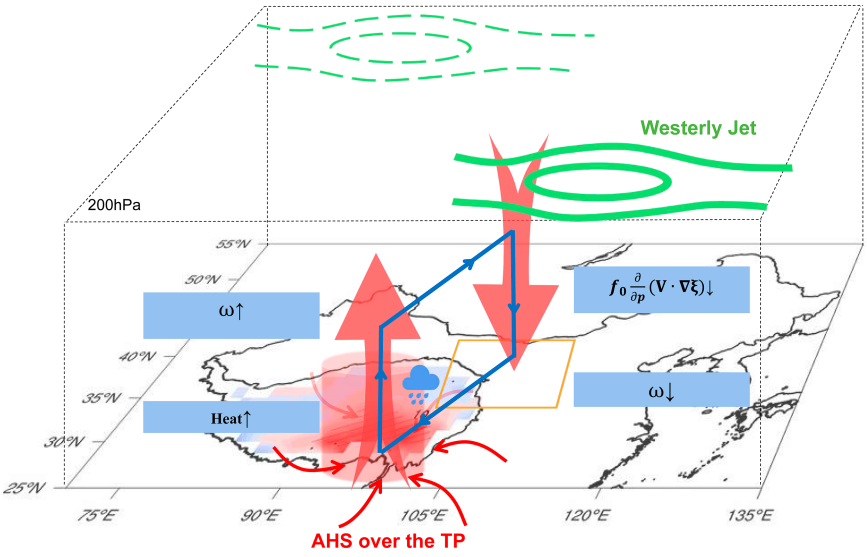

FIG. 17. Schematic diagram of the mechanism of interannual variability of meridional circulation on the north side of the TP. In the figure, Heat ↑ represents the enhanced heating effect of the AHS over the TP in the positive AHS anomalies years, ω ↑ represents the anomalous ascending motion, $f_0(\partial/\partial p)(V\cdot\nabla\xi)$ ↓ represents the negative relative vorticity advection anomaly, and ω↓ represents the anomalous descending motion.

scale teleconnection wave trains along the WJ (Gao et al. 2013). Additionally, the summer AHS over the TP is also influenced by tropical signals, including ENSO (Liu et al. 2020; Hu et al. 2021), Indian Ocean and tropical Pacific SST anomalies, and the Madden–Julian oscillation (Hu and Duan 2015; Chen and You 2017; Sun and Wang 2019; Bai et al. 2023; Zhang and Duan 2023). They can affect the outbreak and development of the Asian summer monsoon system (including the Indian summer monsoon and East Asian summer monsoon), causing changes in the moisture content transported from the tropical ocean to the TP and then influencing the interannual variability of the summer AHS over the TP through the release of LH. Therefore, the multifactor interaction of the summer AHS over the TP, the WJ, other atmospheric circulation systems, and their collective influence on the meridional circulation on the north side of the TP require further study.

Acknowledgments. This work was jointly supported by the National Natural Science Foundation of China (42122034, 42075043, and 42330609), the Science and Technology Program in Gansu (21JR7RA067 and 22ZD6FA005), and the Youth Innovation Promotion Association of Chinese Academy of Sciences (2021427). The authors declare no competing financial interests.

Data availability statement. The Japanese 55-year Reanalysis derived data provided by the Japan Meteorological Agency (JMA) can be downloaded from the website at https://rda.ucar.edu/datasets/ds628.1/dataaccess/. The LBM modeling outputs are available from the corresponding author upon request.

REFERENCES

Bai, L., H.-L. Ren, Y. Wei, Y. Wang, and B. Chen, 2023: Influence of Madden–Julian Oscillation on precipitation over the Tibetan Plateau in boreal summer. *Atmosphere*, **14**, 70, https://doi.org/10.3390/atmos14010070.

Chen, X., and Q. You, 2017: Effect of Indian Ocean SST on Tibetan Plateau precipitation in the early rainy season. *J. Climate*, **30**, 8973–8985, https://doi.org/10.1175/JCLI-D-16-0814.1.

Duan, A., and G. Wu, 2008: Weakening trend in the atmospheric heat source over the Tibetan Plateau during recent decades. Part I: Observations. *J. Climate*, **21**, 3149–3164, https://doi.org/10.1175/2007JCLI1912.1.

——, and P. Zhang, 2022: Interannual variability of atmospheric heat source over the Tibetan Plateau and its driving factors (in Chinese). *Chin. J. Atmos. Sci.*, **46**, 455–472, https://doi.org/10.3878/j.issn.1006-9895.2201.21126.

——, M. Wang, and Z. Xiao, 2014: Uncertainties in quantitatively estimating the atmospheric heat source over the Tibetan Plateau. *Atmos. Oceanic Sci. Lett.*, **7**, 28–33, https://doi.org/10.1080/16742834.2014.11447131.

——, D. Hu, W. Hu, and P. Zhang, 2020: Precursor effect of the Tibetan Plateau heating anomaly on the seasonal march of the East Asian summer monsoon precipitation. *J. Geophys. Res. Atmos.*, **125**, e2020JD032948, https://doi.org/10.1029/2020JD032948.

Fan, G., and G. Cheng, 2003: Simulation of influence of Qinghai-Xizang Plateau uplifting on NW China arid climate forming (II): Changing of atmosphere hydrological cycle and dynamical and thermal effects of plateau (in Chinese). *Plateau Meteor.*, **22**, 58–66.

Flohn, H., 1957: Large-scale aspects of the "summer monsoon" in South and East Asia. *J. Meteor. Soc. Japan*, **35A**, 180–186, https://doi.org/10.2151/jmsj1923.35A.0_180.

Gao, Y., H. Wang, and S. Li, 2013: Influences of the Atlantic Ocean on the summer precipitation of the southeastern

Tibetan Plateau. *J. Geophys. Res. Atmos.*, **118**, 3534–3544, https://doi.org/10.1002/jgrd.50290.

Han, Y., W. Ma, Y. Yang, Y. Ma, Z. Xie, G. Sun, M. Menenti, and B. Su, 2021: Impacts of the Silk Road pattern on the interdecadal variations of the atmospheric heat source over the Tibetan Plateau. *Atmos. Res.*, **260**, 105696, https://doi.org/10.1016/j.atmosres.2021.105696.

He, C., Z. Wang, T. Zhou, and T. Li, 2019: Enhanced latent heating over the Tibetan Plateau as a key to the enhanced East Asian summer monsoon circulation under a warming climate. *J. Climate*, **32**, 3373–3388, https://doi.org/10.1175/JCLI-D-18-0427.1.

Hu, J., and A. Duan, 2015: Relative contributions of the Tibetan Plateau thermal forcing and the Indian Ocean Sea surface temperature basin mode to the interannual variability of the East Asian summer monsoon. *Climate Dyn.*, **45**, 2697–2711, https://doi.org/10.1007/s00382-015-2503-7.

Hu, M., and Q. You, 2019: Characteristics of meridional circulation cell on the South side of Qinghai-Tibetan Plateau and its effects on precipitation over the region (in Chinese). *Plateau Meteor.*, **38**, 14–28, https://doi.org/10.7522/j.issn.1000-0534.2018.00064.

Hu, S., B. Zhou, C. Gao, Z. Xu, Q. Wang, and J. Chou, 2020: Three-pattern decomposition of global atmospheric circulation (in Chinese). *Sci. China: Earth Sci.*, **50**, 1165–1184, https://doi.org/10.1360/SSTe-2019-0229.

——, T. Zhou, and B. Wu, 2021: Impact of developing ENSO on Tibetan Plateau summer rainfall. *J. Climate*, **34**, 3385–3400, https://doi.org/10.1175/jcli-d-20-0612.1.

Kobayashi, S., and Coauthors, 2015: The JRA-55 reanalysis: General specifications and basic characteristics. *J. Meteor. Soc. Japan*, **93**, 5–48, https://doi.org/10.2151/jmsj.2015-001.

Liu, H., K. Duan, M. Li, P. Shi, J. Yang, X. Zhang, and J. Sun, 2015: Impact of the North Atlantic Oscillation on the dipole oscillation of summer precipitation over the central and eastern Tibetan Plateau. *Int. J. Climatol.*, **35**, 4539–4546, https://doi.org/10.1002/joc.4304.

Liu, S., A. Duan, and G. Wu, 2020: Asymmetrical response of the East Asian summer monsoon to the quadrennial oscillation of global sea surface temperature associated with the Tibetan Plateau thermal feedback. *J. Geophys. Res. Atmos.*, **125**, e2019JD032129, https://doi.org/10.1029/2019JD032129.

Liu, Y., Q. Bao, A. Duan, Z. Qian, and G. Wu, 2007: Recent progress in the impact of the Tibetan Plateau on climate in China. *Adv. Atmos. Sci.*, **24**, 1060–1076, https://doi.org/10.1007/s00376-007-1060-3.

Lu, R., and Z. Lin, 2009: Role of subtropical precipitation anomalies in maintaining the summertime meridional teleconnection over the western North Pacific and East Asia. *J. Climate*, **22**, 2058–2072, https://doi.org/10.1175/2008JCLI2444.1.

Luo, H., Z. Wang, S. Yang, and W. Hua, 2023: Revisiting the impact of Asian large-scale orography on the summer precipitation in Northwest China and surrounding arid and semi-arid regions. *Climate Dyn.*, **60**, 33–46, https://doi.org/10.1007/s00382-022-06301-5.

Luo, X., and J. Xu, 2019: Estimate of atmospheric heat source over Tibetan Plateau and its uncertainties (in Chinese). *Climate Change Res.*, **15**, 33–40, https://doi.org/10.12006/j.issn.1673-1719.2018.111.

Peixóto, J. P., and A. H. Oort, 1984: Physics of climate. *Rev. Mod. Phys.*, **56**, 365–429, https://doi.org/10.1103/RevModPhys.56.365.

Qian, Z., T. Wu, and X. Liang, 2001: Feature of mean vertical circulation over the Qinghai-Xizang Plateau and its neighborhood (in Chinese). *Chin. J. Atmos. Sci.*, **25**, 444–454, https://doi.org/10.3878/j.issn.1006-9895.2001.04.02.

Schwendike, J., P. Govekar, M. J. Reeder, R. Wardle, G. J. Berry, and C. Jakob, 2014: Local partitioning of the overturning circulation in the tropics and the connection to the Hadley and Walker circulations. *J. Geophys. Res. Atmos.*, **119**, 1322–1339, https://doi.org/10.1002/2013JD020742.

——, G. J. Berry, M. J. Reeder, C. Jakob, P. Govekar, and R. Wardle, 2015: Trends in the local Hadley and local Walker circulations. *J. Geophys. Res. Atmos.*, **120**, 7599–7618, https://doi.org/10.1002/2014JD022652.

Shang, W., K. Duan, S. Li, X. Ren, and B. Huang, 2021: Simulation of the dipole pattern of summer precipitation over the Tibetan Plateau by CMIP6 models. *Environ. Res. Lett.*, **16**, 014047, https://doi.org/10.1088/1748-9326/abd0ac.

Sun, B., and H. Wang, 2019: Enhanced connections between summer precipitation over the three-river-source region of China and the global climate system. *Climate Dyn.*, **52**, 3471–3488, https://doi.org/10.1007/s00382-018-4326-9.

Sun, H., and X. Liu, 2021: Impacts of dynamic and thermal forcing by the Tibetan Plateau on the precipitation distribution in the Asian arid and monsoon regions. *Climate Dyn.*, **56**, 2339–2358, https://doi.org/10.1007/s00382-020-05593-9.

Sun, J., K. Yang, W. Guo, Y. Wang, J. He, and H. Lu, 2020: Why has the inner Tibetan Plateau become wetter since the mid-1990s? *J. Climate*, **33**, 8507–8522, https://doi.org/10.1175/JCLI-D-19-0471.1.

Wang, C., W. Zhao, and Y. Cui, 2020: Changes in the seasonally frozen ground over the eastern Qinghai-Tibet Plateau in the past 60 years. *Front. Earth Sci.*, **8**, 270, https://doi.org/10.3389/feart.2020.00270.

Wang, M., S. Zhou, and A. Duan, 2012: Trend in the atmospheric heat source over the central and eastern Tibetan Plateau during recent decades: Comparison of observations and reanalysis data (in Chinese). *Chin. Sci. Bull.*, **57**, 548–577, https://doi.org/10.1007/s11434-011-4838-8.

——, D. Guo, and S. Zhong, 2019: Comparison of the multi-source datasets in calculation of the atmospheric heat sources over the Tibetan Plateau (in Chinese). *Meteor. Mon.*, **45**, 1718–1726, https://doi.org/10.7519/j.issn.1000-0526.2019.12.009.

Wang, Z., A. Duan, S. Yang, and K. Ullah, 2017: Atmospheric moisture budget and its regulation on the variability of summer precipitation over the Tibetan Plateau. *J. Geophys. Res. Atmos.*, **122**, 614–630, https://doi.org/10.1002/2016JD025515.

——, S. Yang, N.-C. Lau, and A. Duan, 2018: Teleconnection between summer NAO and East China rainfall variations: A bridge effect of the Tibetan Plateau. *J. Climate*, **31**, 6433–6444, https://doi.org/10.1175/JCLI-D-17-0413.1.

Watanabe, M., and M. Kimoto, 2000: Atmosphere-ocean thermal coupling in the North Atlantic: A positive feedback. *Quart. J. Royal Meteor. Soc.*, **126**, 3343–3369, https://doi.org/10.1002/qj.49712657017.

——, and F.-F. Jin, 2002: Role of Indian Ocean warming in the development of Philippine Sea anticyclone during ENSO. *Geophys. Res. Lett.*, **29**. 1478, https://doi.org/10.1029/2001GL014318.

Wei, F., 2007: *Technology of Statistical Diagnosis and Prediction of Modern Climate* (in Chinese). China Meteorological Press, 296 pp.

Wei, N., Y. Gong, and J. He, 2009: Structural variation of an atmospheric heat source over the Qinghai-Xizang Plateau and its influence on precipitation in Northwest China. *Adv. Atmos. Sci.*, **26**, 1027–1041, https://doi.org/10.1007/s00376-009-7207-7.

Wu, G., W. Li, and H. Guo, 1997: Sensible heat driven air-pump over the Tibetan-Plateau and its impacts on the Asian summer monsoon. *Collections on the Memory of Zhao Jiuzhang* (in Chinese), D. Z. Ye, Ed., Science Press, 116–126.

——, Y. Liu, B. Dong, X. Liang, A. Duan, Q. Bao, and J. Yu, 2012: Revisiting Asian monsoon formation and change associated with Tibetan Plateau forcing: I. Formation. *Climate Dyn.*, **39**, 1169–1181, https://doi.org/10.1007/s00382-012-1334-z.

——, and Coauthors, 2015: Tibetan Plateau climate dynamics: Recent research progress and outlook. *Natl. Sci. Rev.*, **2**, 100–116, https://doi.org/10.1093/nsr/nwu045.

——, B. He, A. Duan, Y. Liu, and W. Yu, 2017: Formation and variation of the atmospheric heat source over the Tibetan Plateau and its climate effects. *Adv. Atmos. Sci.*, **34**, 1169–1184, https://doi.org/10.1007/s00376-017-7014-5.

——, Y. Liu, B. He, Q. Bao, and Z. Wang, 2018: Review of the impact of the Tibetan Plateau sensible heat driven air-pump on the Asian summer monsoon (in Chinese). *Chin. J. Atmos. Sci.*, **42**, 488–504, https://doi.org/10.3878/j.issn.1006-9895.1801.17279.

Wu, T., and Z. Qian, 1996: The comparative analyses of differences between vertical circulation on North side of Tibetan Plateau in wet and dry summer and thermal effects of the plateau (in Chinese). *Acta Meteor. Sin.*, **54**, 558–568, https://doi.org/10.11676/qxxb1996.058.

Xu, X., C. Lu, Y. Ding, X. Shi, Y. Guo, and W. Zhu, 2013: What is the relationship between China summer precipitation and the change of apparent heat source over the Tibetan Plateau? *Atmos. Sci. Lett.*, **14**, 227–234, https://doi.org/10.1002/asl2.444.

Yanai, M., S. Esbensen, and J.-H. Chu, 1973: Determination of bulk properties of tropical cloud clusters from large-scale heat and moisture budgets. *J. Atmos. Sci.*, **30**, 611–627, https://doi.org/10.1175/1520-0469(1973)030<0611:DOBPOT>2.0.CO;2.

Yang, K., X. Guo, and B. Wu, 2010: Recent trends in surface sensible heat flux on the Tibetan Plateau (in Chinese). *Sci. China Earth Sci.*, **54**, 19–28, https://doi.org/10.1007/s11430-010-4036-6.

Ye, D., and Y. Gao, 1979: *Meteorology of the Qinghai-Xizang Plateau* (in Chinese). Science Press, 278 pp.

——, S. Lo, and B. Zhu, 1957: The wind structure and heat balance in the lower troposphere over Tibetan Plateau and its surroundings (in Chinese). *Acta Meteor. Sin.*, **2**, 108–121, https://doi.org/10.11676/qxxb1957.010.

You, Q., F. Wu, L. Shen, N. Pepin, Z. Jiang, and S. Kang, 2020: Tibetan Plateau amplification of climate extremes under global warming of 1.5°C, 2°C and 3°C. *Global Planet. Change*, **192**, 103261, https://doi.org/10.1016/j.gloplacha.2020.103261.

Yu, J., Y. Liu, and G. Wu, 2011: An analysis of the diabatic heating characteristic of atmosphere over the Tibetan Plateau in winter I: Climatology (in Chinese). *Acta Meteor. Sin.*, **69**, 79–88, https://doi.org/10.11676/qxxb2011.007.

Zhang, G., and Coauthors, 2020: Response of Tibetan Plateau lakes to climate change: Trends, patterns, and mechanisms. *Earth-Sci. Rev.*, **208**, 103269, https://doi.org/10.1016/j.earscirev.2020.103269.

Zhang, P., and A. Duan, 2023: Precipitation anomaly over the Tibetan Plateau affected by tropical sea-surface temperatures and mid-latitude atmospheric circulation in September (in Chinese). *Sci. China Earth Sci.*, **66**, 619–632, https://doi.org/10.1007/s11430-022-1067-8.

Zhou, C., P. Zhao, and J. Chen, 2019: The interdecadal change of summer water vapor over the Tibetan Plateau and associated mechanisms. *J. Climate*, **32**, 4103–4119, https://doi.org/10.1175/JCLI-D-18-0364.1.